Monthly Notices of the ROYAL ASTRONOMICAL SOCIETY

MNRAS **472,** 3492–3511 (2017) doi:10.1093/mnras/stx2160
Advance Access publication 2017 August 23

Determining the torus covering factors for a sample of type 1 AGN in the local Universe

Savithri H. Ezhikode,[1]★ Poshak Gandhi,[2] Chris Done,[3] Martin Ward,[3] Gulab C. Dewangan,[4] Ranjeev Misra[4] and Ninan Sajeeth Philip[1]

[1]*Department of Physics, St. Thomas College, Kozhencherry, Kerala 689641, India*
[2]*School of Physics and Astronomy, University of Southampton, Highfield, Southampton SO17 1BJ, UK*
[3]*Centre for Extragalactic Astronomy, Department of Physics, Durham University, South Road, Durham DH1 3LE, UK*
[4]*Inter-University Centre for Astronomy and Astrophysics, Post Bag 4, Ganeshkhind, Pune 411007, India*

Accepted 2017 August 19. Received 2017 August 19; in original form 2016 September 23

ABSTRACT

In the unified scheme of active galactic nuclei, a dusty torus absorbs and then reprocesses a fraction of the intrinsic luminosity which is emitted at longer wavelengths. Thus, subject to radiative transfer corrections, the fraction of the sky covered by the torus as seen from the central source (known as the covering factor f_c) can be estimated from the ratio of the infrared to the bolometric luminosities of the source as $f_c = L_{torus}/L_{Bol}$. However, the uncertainty in determining L_{Bol} has made the estimation of covering factors by this technique difficult, especially for AGN in the local Universe where the peak of the observed spectral energy distributions lies in the UV (ultraviolet). Here, we determine the covering factors of an X-ray/optically selected sample of 51 type 1 AGN. The bolometric luminosities of these sources are derived using a self-consistent, energy-conserving model that estimates the contribution in the unobservable far-UV region, using multifrequency data obtained from SDSS, *XMM–Newton*, *WISE*, 2MASS and UKIDSS. We derive a mean value of $f_c \sim 0.30$ with a dispersion of 0.17. Sample correlations, combined with simulations, show that f_c is more strongly anticorrelated with λ_{Edd} than with L_{Bol}. This points to large-scale torus geometry changes associated with the Eddington-dependent accretion flow, rather than a receding torus, with its inner sublimation radius determined solely by heating from the central source. Furthermore, we do not see any significant change in the distribution of f_c for sub-samples of radio-loud sources or Narrow Line Seyfert 1 galaxies (NLS1s), though these sub-samples are small.

Key words: galaxies: active – galaxies: Seyfert – infrared: galaxies – ultraviolet: galaxies – X-rays: galaxies.

1 INTRODUCTION

Studying broad-band spectral energy distributions (SEDs) of active galactic nuclei (AGN) can shed light on the emission mechanisms operating in the distinct physical components of the AGN. For example, the big blue bump (BBB; Richstone & Schmidt 1980; Sanders et al. 1989; Elvis et al. 1994) in the optical/UV band is associated with modified black body emission from the accretion disc, whereas the Comptonized emission from the corona (Haardt & Maraschi 1993) produces an X-ray power-law continuum above ∼2 keV. Even though the spectral features of various classes of AGN are distinct, the so-called unification scheme (for reviews see Antonucci 1993; Urry & Padovani 1995; Netzer 2015) postulates that the different types of AGN are intrinsically similar. The model suggests the presence of a dusty, molecular torus shaped structure, surrounding the central source, which gives rise to anisotropic emission in polar directions. The observed characteristics of AGN are governed by the orientation of this obscuring torus with respect to our line of sight.

This torus is optically thick, with a size of 0.1–10 pc (Suganuma et al. 2006; Kishimoto et al. 2007; Burtscher et al. 2013). The region has a gas density in the range of 10^4–10^7 cm^{-3} while the column density ranges from $\sim 10^{22}$ to $\sim 10^{25}$ cm^{-2} (Netzer 2013). In the most simple orientation-based unification scheme, the broad-line region may or may not be obscured by the torus material depending on the inclination angle of the system with respect to our line of sight. In this picture, the classification as a type 2 or a type 1 AGN is determined by the orientation alone. The obscuration is parametrized by the opening angle of the torus which in turn

★ E-mail: savithrihezhikode@gmail.com

determines the covering factor f_c. Hence the covering factor is defined as the fraction of the sky that the torus blocks/absorbs the emission from the central source.

The torus is directly exposed to the emission from the central engine and the photons illuminating this region are absorbed by the dust grains. The heated dust then re-radiates these absorbed optical/UV photons in the infrared (IR) band. Hence the IR continuum is attributed to the thermal emission from the silicate and graphite grains with a broad temperature distribution extending up to the sublimation temperatures of about 1500 K. Cooler dust on larger scales emits at longer wavelengths and also shows a silicate feature around ∼10 μm.

Dust grains can no longer survive if heated above their sublimation temperature. As a result, the inner radius of the dust is determined by the distance from the centre, at which the dust is sublimated by the primary continuum. A more luminous AGN heats the dust more strongly and hence the sublimation radius will be larger, with $R \propto L_{\rm Bol}^{1/2}$ (Barvainis 1987). If the dust distribution has a fixed scaleheight (as opposed to scaling with mass and/or mass accretion rate), then this means that the covering factor of the dusty torus decreases as the luminosity of the source increases. This anticorrelation between f_c and the luminosity was suggested by Lawrence (1991) and is called the *receding torus model*. This does not depend on the detailed dust distribution. For example a clumpy torus (Nenkova et al. 2008; Hönig & Kishimoto 2010) would exhibit much the same behaviour as the covering factor is determined mostly by the total solid angle covered by the dust. Similarly, if most of the mid-infrared (MIR) emission arises from scales beyond the classical torus (Hönig et al. 2013; López-Gonzaga et al. 2016; Asmus, Hönig & Gandhi 2016), then f_c would be a measure of the efficiency of this extended emission component and how it scales with AGN power.

There are various methods for determining f_c. One is a statistical approach, based on optical demographic studies of AGN which compared the fraction of type 1 and 2 AGN, with $L_{[OIII]}$ used as a proxy for $L_{\rm Bol}$. Alternatively, this can be done in X-rays, using the fraction of X-ray unobscured to obscured AGN, with $L_{\rm X-ray}$ tracing $L_{\rm Bol}$. Both types of studies generally find a decrease in the fraction of obscured AGN with increasing luminosity, consistent with the receding torus model (e.g. Steffen et al. 2003; Ueda et al. 2003; Hao et al. 2005; La Franca et al. 2005; Simpson 2005; Treister & Urry 2006; Hasinger 2008; Toba et al. 2013; Mateos et al. 2016) but with a few exceptions (Dwelly & Page 2006; Eckart et al. 2006) or additional correlations (Hasinger 2008). However, neither the X-rays nor the optical emission lines, used as proxies, give a reliable estimate of the bolometric luminosity, $L_{\rm Bol}$ (Vasudevan & Fabian 2007; Lusso et al. 2013; Jin et al. 2012a; Jin, Ward & Done 2012b, hereafter J12a, J12b), which is the key driving parameter in the *receding torus model*, and there are also multiple selection effects (Lawrence & Elvis 2010).

Alternatively, the SED can be fitted over as wide a bandpass as possible to directly constrain $L_{\rm Bol}$ from observations, and then the ratio of the IR luminosity to the bolometric luminosity $L_{\rm IR}/L_{\rm Bol}$ can be used to derive f_c based on dust (re)emission. Again, these studies generally show an anticorrelation with $L_{\rm Bol}$ (Gallagher et al. 2007; Maiolino et al. 2007; Hatziminaoglou et al. 2008; Hatziminaoglou, Fritz & Jarrett 2009; Gandhi et al. 2009; Lusso et al. 2013; Roseboom et al. 2013). None the less, there are still uncertainties. A major difficulty in the SED-based analysis is determining the bolometric luminosity of the AGN. A substantial part of the AGN luminosity emerges in the UV region and is unobservable due to the interstellar absorption with our Galaxy. Furthermore, the IR luminosity can be self-obscured, with radiation transfer effects through optically thick dust affecting the IR luminosity observed for type 2 (obscured) objects (Pier & Krolik 1992; Treister, Krolik & Dullemond 2008; Stalevski et al. 2016).

In this work, we use a sample of 51 unobscured AGN, so these should not be affected by radiative transfer effects. They all have well-sampled broad-band optical-UV-X-ray data to define the SED. Additionally, they have $L_{\rm Bol}$ estimated by fits using a self-consistent energy-conserving model to bridge across the unobservable far-UV (FUV) region (J12a, J12b). In this paper, we extend these SEDs to include far-infrared (FIR) wavelengths to estimate the covering factors of the AGN in our sample. We then investigate the dependence of f_c with different AGN properties.

This paper is organised as follows. In Section 2, we discuss the sample selection and preparation of the multiwavelength data. Section 3 gives a detailed description of the modelling of the broad-band SED of the sample. Section 4 deals with the main results obtained in the work. Section 5 is dedicated to the discussion of the results and the conclusions are given in Section 6. The details regarding the local models used in this work, the broad-band SED plot for each source, notes on selected sources, and other relevant information is given in the Appendix. Throughout this paper, we have adopted a cosmology with Hubble constant of $H_0 = 70\,{\rm km\,s^{-1}\,Mpc^{-1}}$, $\Omega_\Lambda = 0.73$ and $\Omega_M = 0.27$.

2 SAMPLE SELECTION AND DATA PREPARATION

For our study, we choose the sample of 51 type 1 AGN analysed by J12a and J12b. These are selected to have good SDSS spectra (DR7) with $z < 0.4$ so that H α and H β lines (black hole mass estimator) are included in the bandpass, and good quality *XMM–Newton* X-ray data are available, without complex absorption features. Optical band continuum points were extracted from the SDSS data by removing line emission, Balmer continuum, and host galaxy contribution. The *XMM–Newton* satellite also has the Optical Monitor (OM) which provides simultaneous optical-UV photometry. These photometric points were extracted using 6 arcsec diameter apertures to minimise host galaxy contamination. Therefore these sources all have well-sampled SEDs, which can be modelled to give a good estimate of their bolometric luminosity. The sample spans a broad range of AGN types comprising 12 Narrow Line Seyfert 1 galaxies (NLS1s), 39 Broad Line Seyfert 1 galaxies (BLS1s), a broad absorption line (BAL) quasar which is also radio-loud (PG 1004+130, No. 13) and two more radio-loud AGN RBS 0875 (No. 14) and PG 1512+370 (No. 45). Further information of these sources is given in table 1 of J12a.

2.1 IR data

We extended the continuum of the SEDs discussed in J12b to include IR data obtained from the *Wide-field Infrared Survey Explorer* (*WISE*; Wright et al. 2010), Two Micron All-Sky Survey (2MASS; Skrutskie et al. 2006) and UKIRT Infrared Deep Sky Survey (UKIDSS) catalogues (Hewett et al. 2006). These span a wavelength range from ∼ 1 μm to 20 μm, giving good coverage from near-infrared (NIR) to MIR wavelengths. For cases where both 2MASS and UKIDSS data were available for each source, we opted to use the UKIDSS data for the NIR band due to its smaller aperture size. Our principal results, and specifically the distribution of covering factors, do not depend on the choice of 2MASS or UKIDSS data, a point which is expanded on in Appendix E. We

Table 1. The bandwidth in μm (Column 3), the effective wavelength $\lambda_{\rm eff}$ in μm (Column 4), the zero-point flux density $F_{\nu 0}$ in Jy (Column 5) to convert from magnitudes and the extinction correction factor (Column 6) for *WISE*, 2MASS & UKIDSS bands.

Survey	Band	Bandwidth μm	$\lambda_{\rm eff}$ μm	$F_{\nu 0}$ Jy	A_λ/A_V
WISE	*W*1	0.663 ± 0.001	3.35 ± 0.01	309.5 ± 4.6	0.069
	*W*2	1.042 ± 0.001	4.60 ± 0.02	171.8 ± 2.5	0.053
	*W*3	5.510 ± 0.020	11.56 ± 0.04	31.7 ± 0.5	0.068
	*W*4	4.100 ± 0.040	22.09 ± 0.12	8.4 ± 0.3	0.052
2MASS	J	0.162 ± 0.001	1.235 ± 0.006	1594.0 ± 27.8	0.282
	H	0.251 ± 0.002	1.662 ± 0.009	1024.0 ± 20.0	0.190
	K	0.262 ± 0.002	2.159 ± 0.011	666.7 ± 12.6	0.114
UKIDSS	Y	0.102	1.031	2026.0	0.380
	J	0.159	1.248	1530.0	0.282
	H	0.292	1.631	1019.0	0.190
	K	0.351	2.201	631.0	0.114

used 2MASS only for sources for which there are no UKIDSS observations. One object in the sample (2XMM J100523.9+410746; No. 12) does not have either UKIDSS or 2MASS data. In that case, we could use only the *WISE* data for the IR analysis. The bandpasses with their zero magnitude flux and aperture sizes are given in Table 1, together with the extinction corrections in each band, A_λ, extracted from Cardelli, Clayton & Mathis (1989) with $R_V = 3.1$ (see Gandhi et al. 2011 and references therein for *WISE* extinction corrections). The resulting NIR–MIR fluxes, corrected for Galactic reddening, are listed in Table 2. We incorporate these into XSPEC using the FTOOL FLX2XSP.

We investigated the dominant IR emission mechanism based on *WISE* colour selection thresholds of Mateos et al. (2012) and Stern et al. (2012). The MIR colour-cut defined by Stern et al. (2012) identifies the AGN candidates with $W1–W2 \geq 0.8$. In addition, the AGN wedge of Mateos et al. (2012) is designed to select objects with red MIR power-law SEDs in the first three bands of *WISE*. Fig. 1 shows that most of the sources in our sample, except 2XMM J100523.9+410746 (No. 12), RX J1140.1+0307 (No. 20), RX J1233.9+0747 (No. 28), 1E 1346+26.7 (No. 36) & NGC 5683 (No. 42), are within the AGN wedge and above the colour-cut. This confirms that the MIR is likely dominated by the AGN rather than the host galaxy in most cases. The MIR fluxes for those which lie below the colour wedge and the colour-cut are likely to be dominated by the stellar population or star formation activity in the host galaxy, especially in the case of *W*1 filter. For example, the MIR SED of NGC 5683 (No. 42) shows a significant contribution from the host galaxy.

3 THE BROAD-BAND SED MODEL

Multiwavelength observations are a crucial ingredient in understanding the physical processes occurring in AGN and to study the structure of their inner regions. Some notable features in the broad-band SED model of AGN are; the hard X-ray power law, the soft X-ray excess below 2 keV, the BBB which peaks in optical/UV region, and the infrared bump at ∼10 μm. The optical/UV emission in AGN is thought to arise from a multitemperature accretion disc. The power-law component originates from the inverse Compton scattering of accretion disc photons by a hot, optically thin corona. The infrared emission results from reprocessing of the absorbed optical/UV/X-ray emission from the AGN.

3.1 Modelling the Optical/UV and X-rays

The SED can be phenomenologically fitted by a black body component for the accretion disc and thermal Comptonization from an optically thin, high-temperature corona to model the hard X-ray power law above 2 keV. At lower wavelengths, the soft X-ray excess can be modelled with an optically thick, low-temperature thermal Comptonization model. In J12b, they modelled the Optical/UV & X-ray continua with the XSPEC model OPTXAGNF[1] (Done et al. 2012). This model is fully self-consistent (energy conserving), and associates all components with emission from the accretion disc itself and energy extracted from it i.e. the soft X-ray component and the hard X-ray power law. OPTXAGNF is parametrized by black hole mass ($M_{\rm BH}$), Eddington ratio ($L/L_{\rm Edd}$ or $\lambda_{\rm Edd}$), black hole spin (a), coronal radius ($R_{\rm cor}$), outer radius of the accretion disc ($R_{\rm out}$), electron temperature ($kT_{\rm e}$) and optical depth (τ) of the corona producing soft X-ray component, hard X-ray (2–10 keV) photon index (Γ), fraction of the coronal energy emitted in the hard X-ray power law ($f_{\rm pl}$) and redshift (z) i.e. 10 parameters in total. In detail, this model introduces $R_{\rm cor}$, the radius down to which the gravitational energy is released as black body emission in the disc. Within this radius, the energy is emitted as the soft X-ray excess and the high energy power law. In this model, the mass accretion rate is constrained by the optical/UV luminosity. If the black hole mass is known, then these parameters can be used to estimate the total luminosity. J12b assumed an accretion efficiency of 0.057 for a Schwarzschild black hole, and hence determined the total luminosity. The study presented in J12b is a refinement to the SED fitting given in J12a. This now includes a self-consistent colour temperature correction for the standard disc emission.

We adopted the same procedures as described in J12b, and performed the spectral analysis of the optical/UV and X-ray continua using OPTXAGNF in XSPEC version 12.8.2. We model the Galactic absorption and reddening using the standard routines *wabs* and *redden*, respectively, and any intrinsic absorption/reddening using *zwabs*/*zredden*. The intrinsic column density was left free to vary during the spectral fitting while the Galactic column density for each source was frozen to the value obtained from Leiden/Argentine/Bonn (LAB) Survey (Kalberla et al. 2005). We fixed the black hole mass to the best-fitting value obtained by J12b in their models, who fixed upper(lower) limits to the mass from the broad(intermediate) velocity width of the H β line decomposition. We also follow the method described in J12a, J12b and fix the outer radius of the accretion disc to be $10^4 R_{\rm g}$. This is probably an upper limit to the size of the disc, as both the self-gravity radius and the best fit to the disc emission generally indicate a somewhat smaller disc (Hao et al. 2010; Collinson et al. 2016). The redshift[2] z is fixed to the value given in Table 2, this leaves nine free parameters for the X-ray fitting portion of the model.

3.2 Modelling the infrared

Our extended wavelength IR coverage is modelled as a combination of dust re-radiation and host galaxy emission. For the dust, we use the Seyfert 1 (unobscured) template of Silva, Maiolino & Granato (2004), and for the host galaxy we use a range of 13 templates spanning ellipticals, spirals and star-forming galaxies, from the Spitzer Wide-Area Infrared Extragalactic survey (SWIRE)

[1] A description of OPTXAGNF can be found in the XSPEC website http://heasarc.nasa.gov/xanadu/xspec/models/optxagn.html.
[2] Redshift for each source is taken from https://ned.ipac.caltech.edu/.

Table 2. Dereddened IR flux for the sample in each band of *WISE*, 2MASS and UKIDSS.

No.	Object	Redshift	IR flux (mJy)										
			WISE				2MASS			UKIDSS			
			W1	*W2*	*W3*	*W4*	*J*	*H*	K_s	*Y*	*J*	*H*	*K*
1	UM 269	0.308	2.10 ± 0.06	2.90 ± 0.07	4.22 ± 0.26	7.94 ± 1.37	0.45 ± 0.05	0.70 ± 0.08	0.93 ± 0.07	–	–	–	–
2	Mrk 1018	0.043	26.58 ± 0.67	30.51 ± 0.72	52.38 ± 1.07	85.36 ± 3.86	8.34 ± 0.58	11.73 ± 0.99	15.35 ± 0.75	–	–	–	–
3	NVSS J030639	0.107	5.15 ± 0.13	6.22 ± 0.15	16.52 ± 0.42	41.50 ± 2.28	–	–	–	1.02 ± 0.03	1.34 ± 0.04	1.99 ± 0.06	2.97 ± 0.09
4	2XMM J074601.2+280732	0.145	1.35 ± 0.04	1.53 ± 0.04	2.43 ± 0.18	3.84 ± 1.19	0.52 ± 0.06	0.66 ± 0.09	0.79 ± 0.08	–	–	–	–
5	2XMM J080608.0+244421	0.358	1.12 ± 0.03	1.56 ± 0.04	3.58 ± 0.22	8.00 ± 1.28	–	–	–	0.25 ± 0.01	0.30 ± 0.01	0.40 ± 0.01	0.56 ± 0.02
6	HS 0810+5157	0.377	1.89 ± 0.05	3.18 ± 0.08	7.99 ± 0.25	21.07 ± 1.51	0.63 ± 0.06	0.87 ± 0.09	1.29 ± 0.09	–	–	–	–
7	RBS 0769	0.160	3.33 ± 0.09	5.36 ± 0.13	15.40 ± 0.39	32.69 ± 1.66	0.90 ± 0.06	1.27 ± 0.11	1.82 ± 0.09	–	–	–	–
8	RBS 0770	0.033	37.65 ± 0.97	45.26 ± 1.07	105.76 ± 2.17	211.87 ± 8.67	10.03 ± 0.46	13.40 ± 0.73	20.01 ± 0.75	–	–	–	–
9	Mrk 0110	0.035	21.67 ± 0.56	29.57 ± 0.70	65.58 ± 1.39	109.36 ± 4.88	4.57 ± 0.23	5.65 ± 0.32	8.58 ± 0.33	–	–	–	–
10	PG 0947+396	0.206	7.93 ± 0.20	12.71 ± 0.3	26.91 ± 0.57	55.27 ± 2.77	1.99 ± 0.08	2.75 ± 0.11	5.34 ± 0.17	–	–	–	–
11	2XMM J100025.2+015852	0.373	0.30 ± 0.01	0.54 ± 0.02	1.47 ± 0.14	4.46 ± 1.05	–	–	–	0.11 ± 0.01	0.11 ± 0.01	0.16 ± 0.01	0.21 ± 0.01
12	2XMM J100523.9+410746	0.206	0.35 ± 0.01	0.50 ± 0.02	0.54 ± 0.15	3.55 ± 0.12	–	–	–	–	–	–	–
13	PG 1004+130	0.241	8.10 ± 0.21	11.90 ± 0.28	36.20 ± 0.79	83.73 ± 4.04	3.41 ± 0.12	3.54 ± 0.16	5.00 ± 0.18	–	–	–	–
14	RBS 0875	0.178	6.72 ± 0.17	8.86 ± 0.21	14.84 ± 0.41	29.33 ± 1.9	1.70 ± 0.10	2.21 ± 0.15	3.58 ± 0.15	–	–	–	–
15	KUG 1031+398	0.043	11.66 ± 0.29	19.32 ± 0.45	70.46 ± 1.40	132.33 ± 5.69	3.57 ± 0.14	4.38 ± 0.21	5.86 ± 0.22	–	–	–	–
16	PG 1048+342	0.167	3.89 ± 0.10	5.58 ± 0.14	13.61 ± 0.34	27.78 ± 1.53	1.28 ± 0.06	1.57 ± 0.08	2.46 ± 0.11	–	–	–	–
17	1RXS J111007	0.262	2.07 ± 0.05	3.08 ± 0.07	8.62 ± 0.27	22.14 ± 1.33	0.33 ± 0.05	0.71 ± 0.07	1.16 ± 0.09	–	–	–	–
18	PG 1115+407	0.155	9.00 ± 0.23	11.54 ± 0.27	24.18 ± 0.53	49.53 ± 2.36	2.21 ± 0.12	3.14 ± 0.18	5.36 ± 0.20	–	–	–	–
19	2XMM J112328.0+052823	0.101	2.64 ± 0.07	3.65 ± 0.09	9.43 ± 0.28	16.42 ± 1.30	–	–	–	0.49 ± 0.02	0.64 ± 0.02	0.96 ± 0.03	1.55 ± 0.05
20	RX J1140.1+0307	0.081	1.35 ± 0.04	1.32 ± 0.04	4.28 ± 0.19	12.06 ± 1.35	–	–	–	0.35 ± 0.01	0.45 ± 0.01	0.65 ± 0.02	–
21	PG 1202+281	0.165	7.41 ± 0.19	10.57 ± 0.25	29.02 ± 0.65	87.03 ± 3.74	2.03 ± 0.08	2.53 ± 0.10	4.82 ± 0.15	–	–	–	–
22	1AXG J121359+1404	0.154	1.06 ± 0.03	1.34 ± 0.04	2.89 ± 0.17	7.57 ± 1.08	–	–	–	0.36 ± 0.01	0.47 ± 0.01	0.61 ± 0.02	0.79 ± 0.02
23	2E 1216+0700	0.080	6.45 ± 0.17	7.79 ± 0.18	17.42 ± 0.46	24.85 ± 1.65	–	–	–	1.28 ± 0.04	1.75 ± 0.05	2.70 ± 0.08	3.90 ± 0.12
24	1RXS J122019	0.286	2.08 ± 0.06	3.06 ± 0.08	5.66 ± 0.20	7.83 ± 1.09	0.52 ± 0.06	0.78 ± 0.10	1.35 ± 0.11	–	–	–	–
25	LBQS 1228+1116	0.236	3.08 ± 0.08	4.68 ± 0.12	11.17 ± 0.28	30.99 ± 1.86	–	–	–	0.96 ± 0.03	0.99 ± 0.03	1.29 ± 0.04	1.56 ± 0.05
26	2XMM J123126.4+105111	0.304	0.49 ± 0.02	0.66 ± 0.02	1.71 ± 0.17	2.39 ± 0.91	–	–	–	0.12 ± 0.00	0.14 ± 0.01	0.19 ± 0.01	0.33 ± 0.01
27	Mrk 0771	0.064	13.34 ± 0.35	18.42 ± 0.43	57.38 ± 1.17	159.39 ± 6.68	4.63 ± 0.26	6.15 ± 0.37	9.46 ± 0.39	–	–	–	–
28	RX J1233.9+0747	0.371	0.51 ± 0.02	0.48 ± 0.02	1.09 ± 0.18	5.33 ± 0.19	–	–	–	0.11 ± 0.00	0.15 ± 0.01	0.19 ± 0.01	0.24 ± 0.01
29	RX J1236.0+2641	0.209	3.08 ± 0.08	4.61 ± 0.11	13.12 ± 0.37	37.95 ± 1.98	0.74 ± 0.05	1.04 ± 0.08	1.66 ± 0.08	–	–	–	–
30	PG 1244+026	0.048	6.86 ± 0.17	10.03 ± 0.24	41.53 ± 0.88	114.83 ± 4.87	–	–	–	1.34 ± 0.04	1.58 ± 0.05	2.15 ± 0.06	3.23 ± 0.10
31	2XMM J125553.0+272405	0.316	1.13 ± 0.03	1.36 ± 0.04	2.39 ± 0.17	6.37 ± 0.93	–	–	–	0.28 ± 0.01	0.35 ± 0.01	0.51 ± 0.02	0.78 ± 0.02
32	RBS 1201	0.091	3.20 ± 0.08	3.59 ± 0.09	8.29 ± 0.25	19.65 ± 1.43	–	–	–	1.03 ± 0.03	1.27 ± 0.04	1.74 ± 0.05	1.92 ± 0.06
33	2XMM J132101.4+340658	0.334	0.77 ± 0.02	0.94 ± 0.03	1.73 ± 0.11	3.93 ± 0.78	0.31 ± 0.05	0.29 ± 0.06	0.61 ± 0.08	–	–	–	–
34	1RXS J132447	0.306	1.65 ± 0.05	2.23 ± 0.06	4.21 ± 0.18	11.40 ± 1.06	–	–	–	0.82 ± 0.03	0.84 ± 0.03	0.96 ± 0.03	1.19 ± 0.04
35	UM 602	0.237	3.74 ± 0.10	5.19 ± 0.13	8.34 ± 0.23	18.25 ± 1.31	–	–	–	0.52 ± 0.02	0.57 ± 0.02	0.80 ± 0.02	1.47 ± 0.04
36	1E 1346+26.7	0.059	4.34 ± 0.13	4.87 ± 0.13	18.74 ± 0.42	34.30 ± 1.86	–	–	–	1.09 ± 0.03	1.40 ± 0.04	2.12 ± 0.06	2.66 ± 0.08
37	PG 1352+183	0.151	7.09 ± 0.18	10.07 ± 0.24	18.03 ± 0.41	35.78 ± 1.80	1.61 ± 0.08	2.11 ± 0.10	3.78 ± 0.14	–	–	–	–
38	Mrk 0464	0.050	3.69 ± 0.10	5.03 ± 0.12	14.32 ± 0.34	28.24 ± 1.59	1.94 ± 0.08	2.33 ± 0.10	3.04 ± 0.12	–	–	–	–
39	1RXS J135724	0.106	0.78 ± 0.02	1.00 ± 0.03	3.51 ± 0.12	15.31 ± 1.16	0.28 ± 0.05	0.53 ± 0.08	0.59 ± 0.09	–	–	–	–
40	PG 1415+451	0.114	10.39 ± 0.27	13.31 ± 0.31	29.32 ± 0.62	64.93 ± 2.93	3.80 ± 0.12	5.59 ± 0.19	8.69 ± 0.27	–	–	–	–
41	PG 1427+480	0.221	3.64 ± 0.09	5.57 ± 0.13	14.18 ± 0.33	46.39 ± 2.24	1.33 ± 0.07	1.68 ± 0.10	2.76 ± 0.12	–	–	–	–
42	NGC 5683	0.037	5.37 ± 0.14	4.96 ± 0.12	19.55 ± 0.45	50.03 ± 2.32	5.46 ± 0.27	6.47 ± 0.37	7.10 ± 0.29	–	–	–	–
43	RBS 1423	0.208	3.80 ± 0.10	5.74 ± 0.14	12.26 ± 0.31	25.90 ± 1.56	–	–	–	0.50 ± 0.02	0.70 ± 0.02	0.99 ± 0.03	1.94 ± 0.06
44	PG 1448+273	0.065	11.35 ± 0.29	15.10 ± 0.36	45.53 ± 0.93	117.29 ± 4.92	5.64 ± 0.19	7.29 ± 0.24	10.29 ± 0.31	–	–	–	–
45	PG 1512+370	0.371	4.18 ± 0.10	6.67 ± 0.16	13.84 ± 0.33	34.36 ± 1.61	1.09 ± 0.06	1.36 ± 0.08	2.26 ± 0.12	–	–	–	–
46	Q 1529+050	0.218	2.18 ± 0.06	2.92 ± 0.07	6.03 ± 0.20	19.48 ± 1.48	–	–	–	0.40 ± 0.01	0.52 ± 0.02	0.68 ± 0.02	1.24 ± 0.04
47	1E 1556+27.4	0.090	1.90 ± 0.05	2.08 ± 0.05	4.01 ± 0.16	6.93 ± 0.83	–	–	–	0.85 ± 0.03	1.22 ± 0.04	1.34 ± 0.04	1.61 ± 0.05
48	Mrk 0493	0.031	19.93 ± 0.51	24.46 ± 0.58	72.03 ± 1.43	162.81 ± 6.67	6.00 ± 0.29	8.21 ± 0.45	10.65 ± 0.44	–	–	–	–
49	IIZw 177	0.081	3.79 ± 0.10	4.72 ± 0.11	20.70 ± 0.48	60.99 ± 2.76	1.77 ± 0.09	2.56 ± 0.13	2.91 ± 0.15	–	–	–	–
50	PG 2233+134	0.326	5.25 ± 0.13	8.26 ± 0.20	20.97 ± 0.50	57.39 ± 2.92	0.99 ± 0.06	1.18 ± 0.07	2.03 ± 0.12	–	–	–	–
51	Mrk 0926	0.047	69.60 ± 1.80	86.16 ± 2.03	123.69 ± 2.53	256.37 ± 10.75	8.97 ± 0.36	12.43 ± 0.49	17.00 ± 0.64	–	–	–	–

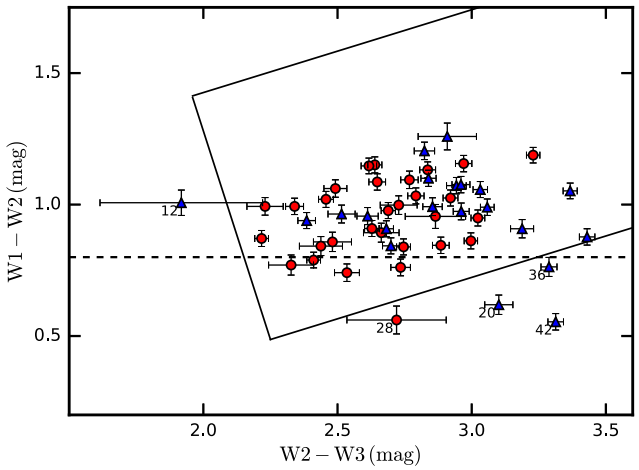

Figure 1. *WISE* colour–colour plot for our sample. The solid line describes the AGN wedge Mateos et al. (2012) and the colour-cut Stern et al. (2012) is plotted with the dashed line. Blue triangles denote objects with significant host galaxy contribution ($L_{\rm host} > 10$ per cent of $L_{\rm Bol}$) in the model fit.

library (Polletta et al. 2007). We incorporate these into XSPEC as local models, which we call *agndust* and *hostpol*. Further details of *agndust* and *hostpol* templates are given in Appendix A. We use only the Seyfert 1 dust template in our fits since all our objects are unobscured, but we do investigate the entire range of host galaxy templates, and then adopt the one which gives the best fit to each object. The optical/UV, X-ray and IR continua of each source in the sample were fitted by the final model *constant*(*hostpol* + *agndust* + *wabs* × *redden* × *zwabs* × *zredden* × OPTXAGNF), where the *constant* only allows for small cross-calibration differences in normalization between the X-ray spectra obtained from the three independent cameras EPIC-pn, MOS1 and MOS2, aboard the *XMM–Newton* satellite. The broad-band SED model for each source has 11 free parameters (including the normalizations of *agndust* and *hostpol*), apart from the multiplicative factor of the model *constant*. The fit-statistic and the best-fitting hostpol template for each source are given in Table 3. The plots showing the data and individual model components for all the sources are given in Appendix B. Mrk 0110 (No. 9) shows a clear discrepancy in the SDSS data due to extreme variability, and therefore has a very large χ^2. Also, there are two super-Eddington sources in our sample, KUG 1031+398 (No. 15) and PG 2233+134 (No. 50). These sources are discussed individually in Appendix C. We note that the potential discrepancies mentioned above do not influence any of our resulting inferences on the f_c distribution.

4 RESULTS

4.1 Broad-band SEDs and covering factors

Our best-fitting model parameters for the SED fits are given in Table 3. We integrate the intrinsic OPTXAGNF model (after correcting for all absorption components) over the energy range of 10^{-6}–100 keV ($\sim 10^{-5}$–1000 μm) to obtain $L_{\rm Bol}$, and over 2–10 keV to get the hard X-ray luminosity $L_{\rm X-ray}$. Now, in order to estimate the covering factor we can compare these to the IR luminosity of the torus $L_{\rm torus}$, which we find by integrating the *agndust* model component over ∼1–1000 μm. We also give the luminosity of the host galaxy $L_{\rm host}$, obtained by integrating the host galaxy template over ∼0.1–1000 μm, and give its type in Table 3. The distributions of these luminosities are shown in Fig. 2. The bolometric luminosities of most of the sources in our study are lower than the values of J12b by a factor of ∼1.7. This is due to a change in energy grid handling of OPTXAGNF in an older version of XSPEC.[3] Though individual $L_{\rm Bol}$ values are affected, the overall sample trends remain the same. The host galaxy is significantly detected in 38 sources. We note that the host galaxy morphological types of 21 sources in our sample are known from the literature and many of these (No. 8, 13, 15, 16, 20, 21, 23, 27, 30, 37, 38, 39, 42, 44, 48, 50) are different to those indicated by our best fit. We have refit these objects using the galaxy template fixed to the literature values. Although there is a marginal increase in χ^2 when using the substituted templates, this has no significant impact on the parameters derived for either the AGN or the torus.

The primary goal of this work is to determine the distribution of covering factors f_c of the unobscured AGN sample. This distribution of f_c obtained from the ratio of the torus luminosity to the bolometric luminosity is given in Fig. 3. The distribution, with an average value around 0.30, has a scatter of ∼0.17. The source with the minimum covering factor is 1E 1556+27.4 (No. 47). The value of f_c ∼0.02 suggests that this source could be a *hot-dust-poor* AGN (Hao et al. 2010) characterized by weak IR emission. At the opposite extreme, 2E 1216+0700 (No. 23) has the maximum value of f_c (∼0.88).

4.2 Comparison with previous work

Many previous studies have discussed the obscured AGN fraction. Lawrence & Elvis (2010) reviewed the studies that dealt with the fraction of obscured AGN and concluded that the obscured fraction for the non-X-ray selected samples has a mean value of about 0.58 with a dispersion of ∼0.05. They also gave a rough estimate of 0.53 for the obscured fraction using the updated *Swift*/BAT hard X-ray catalogue (Tueller et al. 2010), after applying the correction for missing Compton thick objects (Risaliti, Maiolino & Salvati 1999). The covering factors of a sample of 5281 *WISE*, UKIDSS and SDSS selected high luminosity quasars ($L_{\rm Bol} > 10^{46}$ erg s^{-1}) with redshift <1.5 was determined by Roseboom et al. (2013). They found that the covering factors (estimated by using the ratio of IR to UV/optical luminosity) obey a log-normal distribution with a mean observed value of ∼0.39 and a dispersion of ∼0.2. The study by Lusso et al. (2013) estimated the covering factor for a sample of X-ray selected type 1 AGN with an even wider span of redshifts ($0.10 \leq z \leq 3.75$). They determined the covering factor of the optically thin torus and this was observed to be in the range from ∼0.45 to ∼0.75. In comparison, the result from our sample is relatively low, especially since our sample is comprised only of Seyfert type 1 objects, so radiative transfer corrections, which reduce f_c due to the torus being optically thick to its own radiation at high inclination, should not be important (but see Stalevski et al. 2016). At high luminosities, two other studies, Mor & Trakhtenbrot (2011) and Landt et al. (2011), concentrated on the hot (NIR-emitting) dust component and found even lower hot dust covering factors of ∼0.13 and ∼0.07, respectively.

In Appendix D, we investigate the effect of varying the template SEDs on the f_c measurements. In particular, we examined the impact of using two other IR SEDs for type 1 AGN –(1) proposed by Mullaney et al. (2011) based upon observations of local sources

[3] See the XSPEC patch 12.8.2j available at: https://heasarc.gsfc.nasa.gov/docs/xanadu/xspec/issues/archive/issues.12.8.2q.html.

Table 3. Broad-band SED fitting results. *hostpol* model: best-fitting *hostpol* template (*starburst galaxies); χ^2_{red}: reduced χ^2 for the best-fitting model; N_H^{Gal} & N_H^{Int}: Galactic and intrinsic column densities, respectively, in 10^{20} cm^{-2}; M_{BH}: black hole mass in 10^7 M$_\odot$ (fixed to the best-fitting values of J12b); λ_{Edd}: Eddington ratio; R_{cor}: coronal radius in R_g; kT_e: electron temperature for the soft Comptonization component in keV; τ: optical depth of the soft Comptonization component; Γ: hard X-ray photon index; f_{pl}: fraction of the power below R_{cor} emitted in the hard Comptonization component; L_{X-ray}: unabsorbed X-ray luminosity in the band of 2–10 keV; L_{host}: host galaxy luminosity in the ∼0.1–1000 μm band; L_{torus}: infrared (∼1–1000 μm) luminosity of the torus emission; L_{Bol}: bolometric luminosity in the range of 10^{-6}–100 keV; κ_{2-10}: hard X-ray bolometric correction (L_{Bol}/L_{X-ray}); f_c: Covering factor, the ratio of L_{torus} and L_{Bol}. All luminosities are expressed in 10^{44} erg s^{-1}.

No.	*hostpol* model	χ^2_{red}	N_H^{Gal} 10^{20}cm^{-2}	N_H^{Int} 10^{20}cm^{-2}	M_{BH} 10^7 M$_\odot$	λ_{Edd}	R_{cor} R_g	kT_e keV	τ	Γ	f_{pl}	L_{X-ray} 10^{44} erg s^{-1}	L_{host} 10^{44} erg s^{-1}	L_{torus} 10^{44} erg s^{-1}	L_{Bol} 10^{44} erg s^{-1}	κ_{2-10}	f_c
1	E5	1.34	1.79	3.43	41.00	0.11	97.0	0.11	28.1	1.85	0.49	3.0	<0.5	14.9	41.6	13.74	0.36
2	S0	1.99	2.43	1.29	6.92	0.08	94.2	0.19	16.9	1.82	0.36	0.4	0.6	1.9	8.3	18.80	0.23
3	S0	1.34	6.31	0.66	4.07	0.20	12.6	0.18	15.2	1.87	0.82	0.3	0.9	3.9	10.1	37.94	0.38
4	IRAS 22491−1808*	1.23	3.49	2.69	60.00	0.01	84.3	0.34	14.3	1.67	0.45	0.5	<0.4	0.9	8.0	17.28	0.12
5	S0	1.29	3.53	8.08	8.71	0.97	34.8	0.20	14.3	2.16	0.15	1.0	1.6	13.1	72.0	71.60	0.18
6	IRAS 22491−1808*	1.39	4.24	0.00	31.40	0.29	21.0	0.42	11.0	1.85	0.45	2.4	17.1	28.8	73.8	30.90	0.40
7	IRAS 22491−1808*	1.20	1.33	0.00	3.80	0.99	10.5	0.15	32.7	2.20	0.31	0.2	3.7	7.7	42.7	178.10	0.18
8	S0	1.89	3.12	3.80	3.47	0.29	21.7	0.18	14.4	1.80	0.51	0.5	0.2	2.2	14.1	26.42	0.16
9	Sa	19.62	1.30	0.00	2.51	0.65	17.4	0.26	15.5	1.73	0.83	1.0	–	1.4	22.5	22.70	0.06
10	S0	1.70	1.74	1.01	21.90	0.38	39.5	0.49	9.6	1.76	0.28	2.7	<0.2	27.9	87.0	32.33	0.32
11	IRAS 20551−4250*	1.00	1.72	0.00	8.32	0.38	23.1	0.45	12.3	1.54	0.84	1.0	8.1	4.1	22.8	23.05	0.18
12	S0	1.17	1.20	0.00	6.61	0.05	19.3	0.10	54.1	1.94	0.88	0.2	0.7	1.1	3.5	17.81	0.30
13	IRAS 22491−1808*	1.92	3.56	0.00	158.49	0.07	9.9	0.19	15.0	1.45	0.93	0.5	62.1	34.5	104.5	193.86	0.33
14	S0	1.47	1.76	0.00	17.38	0.11	100.0	0.23	20.3	1.77	0.81	2.4	2.5	12.6	19.3	7.95	0.65
15	Sd	1.67	1.31	2.81	0.20	2.64	100.0	0.30	8.7	2.20	0.03	0.04	0.8	1.8	7.8	190.64	0.23
16	IRAS 22491−1808*	1.50	1.70	2.21	19.95	0.18	28.9	0.30	13.0	1.74	0.34	1.2	<1.3	8.1	39.6	34.33	0.20
17	Arp 220*	1.06	0.65	1.13	6.17	0.51	93.8	0.48	9.0	1.61	0.12	0.4	18.0	13.6	30.9	72.26	0.44
18	E5	1.82	1.45	0.00	13.18	0.61	11.6	0.25	14.0	2.20	0.47	1.0	<0.1	13.4	91.9	94.83	0.15
19	S0	1.00	3.70	0.00	5.10	0.04	69.1	0.16	20.6	1.94	0.21	0.1	0.3	2.0	2.5	36.39	0.78
20	Sd	1.24	1.91	0.00	0.63	0.19	18.0	0.20	22.5	2.20	0.57	0.1	0.5	0.5	1.6	30.18	0.30
21	M 82*	3.82	1.77	0.00	9.60	0.46	23.7	0.21	18.6	1.77	0.78	3.0	<0.1	17.6	48.6	16.27	0.36
22	S0	1.21	2.75	4.37	6.90	0.08	77.7	0.12	23.1	1.82	0.33	0.3	0.6	1.7	6.6	21.68	0.25
23	S0	2.10	1.59	0.00	10.00	0.02	100.0	0.36	14.1	1.52	0.49	0.1	0.7	2.3	2.6	20.23	0.88
24	S0	2.90	1.63	0.00	18.00	0.15	39.8	0.22	25.1	1.91	0.95	2.6	2.1	13.7	23.9	9.32	0.57
25	IRAS 22491−1808*	2.00	2.34	0.01	26.92	0.33	16.2	0.34	13.0	1.79	0.52	2.3	<4.6	12.9	87.2	38.79	0.15
26	S0	1.20	2.31	6.50	5.01	0.76	16.5	0.35	9.2	2.01	0.1	0.2	0.3	4.1	34.5	171.75	0.12
27	IRAS 22491−1808*	1.68	2.75	1.59	7.24	0.16	28.3	0.11	20.1	2.20	0.29	0.3	4.5	3.9	15.8	47.15	0.24
28	S0	1.64	1.45	5.55	9.12	0.67	75.3	0.37	10.6	1.69	0.22	1.4	0.6	4.9	50.0	36.17	0.10
29	Arp 220*	1.23	1.18	1.31	7.41	0.46	12.9	0.15	15.0	2.18	0.45	0.5	21.2	11.9	35.6	73.93	0.34
30	IRAS 22491−1808*	1.24	1.87	0.00	1.86	0.20	19.0	0.23	19.3	2.20	0.46	0.1	4.2	1.1	5.3	36.96	0.21
31	Sb	1.55	0.84	0.00	50.00	0.06	100.0	0.40	14.2	1.45	0.74	1.4	<0.7	8.1	19.9	14.59	0.41
32	S0	1.64	0.90	0.00	4.17	0.11	100.0	0.34	13.3	1.85	0.49	0.4	0.6	1.5	5.7	13.23	0.26
33	S0	2.05	1.07	0.00	8.32	0.33	13.6	0.20	20.2	2.19	0.79	0.6	0.8	6.9	23.3	39.45	0.29
34	S0	1.48	1.83	1.96	51.00	0.06	54.7	0.23	16.4	1.87	0.40	1.4	5.3	10.9	28.6	20.36	0.38
35	S0	2.67	1.76	0.00	4.64	0.90	77.5	0.31	18.4	1.90	0.97	6.2	1.4	13.6	41.0	6.67	0.33
36	Sb	1.43	1.18	2.48	1.00	0.20	25.6	0.44	7.9	2.19	0.34	1.0	0.4	1.0	2.8	36.25	0.35
37	Sa	1.84	1.82	0.98	17.00	0.18	93.1	0.16	20.1	2.12	0.39	1.4	0.3	9.8	37.2	26.10	0.26
38	S0	1.56	1.42	0.65	6.17	0.01	100.0	0.23	14.1	1.72	0.90	0.2	0.2	0.6	1.1	7.31	0.55
39	Arp 220*	1.01	1.36	1.45	2.19	0.08	91.9	0.22	17.5	2.08	0.35	0.1	4.2	0.6	2.2	25.06	0.27
40	S0	2.15	0.77	0.00	7.59	0.20	15.5	0.35	11.7	1.93	0.45	0.4	2.5	8.4	19.2	45.35	0.44
41	IRAS 22491−1808*	1.48	1.81	0.82	13.80	0.59	14.0	0.39	11.0	1.86	0.51	1.8	17.3	15.1	83.8	47.91	0.18
42	Sc	2.56	2.86	0.00	5.50	0.02	47.9	0.24	15.0	1.89	0.79	0.1	0.6	0.3	1.3	10.42	0.22
43	IRAS 22491−1808*	1.54	2.69	0.23	12.00	0.36	100.0	0.29	13.3	1.87	0.46	3.2	<0.4	12.9	46.2	14.28	0.28
44	E2	1.44	2.78	4.11	3.63	0.71	12.7	0.33	10.0	2.14	0.2	0.2	1.7	3.2	35.0	150.67	0.09
45	IRAS 20551−4250*	2.54	1.46	2.26	60.26	0.42	49.7	0.20	16.9	1.93	0.37	9.3	<1.5	51.9	212.0	22.85	0.24
46	IRAS 22491−1808*	1.59	4.02	11.36	36.00	0.06	100.0	0.11	31.5	1.93	0.40	1.4	<2.6	7.2	24.4	18.07	0.30
47	E2	1.41	3.78	17.63	9.05	0.19	100.0	0.11	29.7	1.87	0.20	0.7	<0.1	0.6	23.2	33.66	0.02
48	S0	1.42	2.11	0.00	2.95	0.09	35.1	0.37	11.6	1.91	0.24	0.1	0.2	1.2	3.7	38.05	0.32
49	M 82*	1.51	4.90	0.00	5.30	0.07	100.0	0.19	24.4	2.20	0.50	0.2	3.7	1.4	4.7	25.65	0.30
50	IRAS 22491−1808*	5.17	4.51	0.00	23.99	2.07	9.3	0.62	7.3	2.20	0.46	2.0	<20.5	49.4	430.3	216.60	0.11
51	S0	2.25	2.91	0.87	3.98	0.19	100.0	0.13	39.6	1.78	0.96	1.5	0.4	5.9	9.8	6.51	0.60

in which the AGN dominates the IR portion of the SED over the host galaxy contribution; and (2) a theoretical clumpy torus SED by Hönig & Kishimoto (2010). While the resultant mean f_c value and the distribution of values from these template fits do not dramatically differ from those obtained previously when we used the SEDs from Silva et al. (2004), we found that both these sets of templates required an additional hot dust component in the NIR regime, suggesting that they are too restricted to account for the broad-band features in our observations. This finding is interesting, but further investigation is beyond the scope of this paper. However, we note that similar hot dust components are required in other quasar SED studies (e.g. Mor et al. 2009).

4.3 f_c in sub-samples

From our main sample, we have constructed sub-samples of three radio-loud objects and 12 NLS1 galaxies. The distributions of covering factor for these sub-samples are shown in Fig. 3.

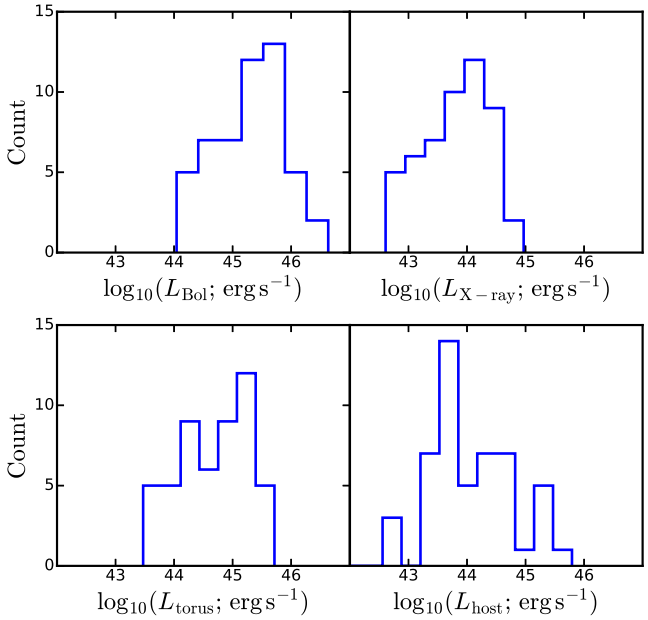

Figure 2. The distribution of $L_{\rm Bol}$ (upper left), $L_{\rm X-ray}$ (2–10 keV) (upper right), $L_{\rm torus}$ (lower left) and $L_{\rm host}$ (lower right).

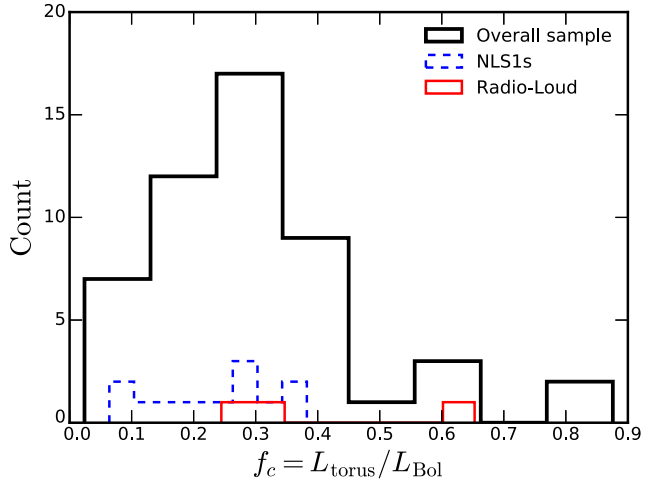

Figure 3. Histogram of covering factors for the sample of 51 type 1 AGN (thick black line) and the sub-samples of 12 NLS1s (dashed blue line) and 3 radio-loud sources (thin red line).

4.3.1 Radio-loud sources

A significant contribution from a jet may reduce the covering factor in radio-loud sources. One of these objects in our sample, PG 1004+130 (No. 13), is a BAL quasar with a very weak X-ray spectrum. J12b suggests that the origin of X-rays in this source could be a sub-parsec-scale jet. However, the covering factors of the three radio-loud objects (No. 13, No. 14 & No. 45) in our sample are 0.33, 0.65 and 0.24, respectively, indicating that the covering factors may not be affected by the radio-loudness/quietness of the sources, although we cannot draw general conclusions from such a small sample of radio-loud sources.

4.3.2 NLS1 galaxies

It is known that the NLS1s, in general, tend to have higher values of Eddington ratio. Since there is an anticorrelation between $f_{\rm c}$ and $\lambda_{\rm Edd}$ we expect the 12 NLS1s in our sample to have low values for $f_{\rm c}$. The covering factors of NLS1s in our sample range from ∼0.06 to ∼0.38 with a mean value around 0.23 and a dispersion of about 0.1. The Kolmogorov–Smirnov test (K–S test) with a probability of ∼75.5 per cent reveals that the distribution of $f_{\rm c}$ in NLS1s does not differ significantly from that of the overall sample. But we caution that no strong statement can be made, based on such a small sub-sample of NLS1s. We need further investigations to get better constraints on this result.

4.4 Correlations obtained

J12b carried out a systematic study of the correlation between the different AGN parameters in this sample. We follow J12b, but also include the new torus parameters, $L_{\rm torus}$ and covering fraction $f_{\rm c}$ and compute the correlations using the Spearman's rank-order method (Press et al. 1992). The rank coefficient ρ_s and probability d_s (also known as the p-value) for the Spearman's correlation between different parameters are listed in Table 4. We recover most of the correlations, obtained by J12b, between $L_{\rm Bol}$, $\lambda_{\rm Edd}$, Γ and the hard X-ray bolometric correction κ_{2-10} defined as $L_{\rm Bol}/L_{\rm X-ray}$ (Vasudevan & Fabian 2007). Additionally, we find a marginal correlation of $f_{\rm c}$ with $L_{\rm Bol}$ ($d_s = 0.05$) and a stronger correlation between $f_{\rm c}$ and $\lambda_{\rm Edd}$ ($d_s = 0.002$). But $f_{\rm c}$ shows no significant correlation with $L_{\rm X-ray}$ or $L_{\rm torus}$, as shown in Fig. 4.

J12b suggest that the combination of $\lambda_{\rm Edd}$ and $M_{\rm BH}$ drives the correlations seen in the AGN parameters, with $\lambda_{\rm Edd}$ changing the accretion flow geometry (resulting in the correlations in Γ, $R_{\rm cor}$ and $f_{\rm pl}$ which drive the correlation with κ_{2-10}) while $M_{\rm BH}$ and $\lambda_{\rm Edd}$ together set the overall luminosity and the peak temperature of the disc. As $f_{\rm c}$ correlates with $\lambda_{\rm Edd}$ and $L_{\rm Bol} \propto {\rm M_{BH}}\lambda_{\rm Edd}$ then it is clear that the correlations of $f_{\rm c}$ with $\lambda_{\rm Edd}$ and $L_{\rm Bol}$, shown in Fig. 4, will also give rise to correlations of $f_{\rm c}$ with the other AGN parameters. However, the major statistical correlation with the new torus parameters is that $f_{\rm c}$ correlates with $\lambda_{\rm Edd}$ and $L_{\rm Bol}$. This is in accord with the physical expectations that $\lambda_{\rm Edd}$ and $L_{\rm Bol}$ are the two key parameters which determine the properties of the accretion flow.

There is also a weak correlation between $L_{\rm host}$ and $M_{\rm BH}$. This is expected from the black hole mass and bulge luminosity ($L_{\rm Bulge}$) relation of Magorrian et al. (1998). Since the SED of a normal galaxy stellar population peaks in the H band, we calculated the corresponding luminosity for our sample in terms of $L_{\rm host}$ and the relative H-band flux from Polletta et al. (2007) SED templates. Here, we are not considering Mrk 0110 (No. 9) since $L_{\rm host}$ is not well constrained for this source. We find that the sources in which our SED fits include a significant host galaxy contribution approximately follow the Magorrian relationship, though there is significant scatter (∼0.5 dex) between $M_{\rm BH}$ and $L_{\rm Bulge}$ (see Fig. 5). This shows that our host galaxy fitted components are largely reasonable. Here, we note that among the 13 sources for which there is no significant host galaxy contribution, most of them are fitted by starburst galaxy templates (e.g. No. 50, No. 16). These starburst templates peak in the FIR and show a minimum around NIR wavelengths. Since our SEDs do not cover the FIR wavelengths and the starbursts tend to be extended we may be underestimating their FIR emission, and also their bulge luminosities. In these few cases, we cannot rule out that we are then overestimating the torus contribution and hence

Table 4. Spearman's correlation between different parameters.

Parameter 1	Parameter 2	ρ_s	d_s
$\lambda_{\rm Edd}$	$M_{\rm BH}$	−0.17	0.24
$\lambda_{\rm Edd}$	$L_{\rm Bol}$	0.61	1.64×10^{-06}
$\lambda_{\rm Edd}$	$L_{\rm X-ray}$	0.28	0.04
$\lambda_{\rm Edd}$	$L_{\rm torus}$	0.439	0.001
$\lambda_{\rm Edd}$	κ_{2-10}	0.54	4.49×10^{-05}
$\lambda_{\rm Edd}$	$R_{\rm cor}$	−0.47	5.41×10^{-05}
$\lambda_{\rm Edd}$	$f_{\rm pl}$	−0.234	0.099
$\lambda_{\rm Edd}$	Γ	0.26	0.06
$\lambda_{\rm Edd}$	$f_{\rm c}$	−0.428	0.002
$L_{\rm Bol}$	$L_{\rm X-ray}$	0.76	7.8×10^{-11}
$L_{\rm Bol}$	$L_{\rm torus}$	0.87	1.15×10^{-16}
$L_{\rm Bol}$	κ_{2-10}	0.34	0.02
$L_{\rm Bol}$	$R_{\rm cor}$	−0.368	0.008
$L_{\rm Bol}$	$f_{\rm pl}$	−0.08	0.56
$L_{\rm Bol}$	Γ	−0.08	0.57
$L_{\rm Bol}$	$f_{\rm c}$	−0.27	0.05
$M_{\rm BH}$	$L_{\rm Bol}$	0.61	2.16×10^{-06}
$M_{\rm BH}$	$L_{\rm X-ray}$	0.69	1.71×10^{-08}
$M_{\rm BH}$	$L_{\rm torus}$	0.65	2.66×10^{-07}
$M_{\rm BH}$	κ_{2-10}	−0.13	0.35
$M_{\rm BH}$	$R_{\rm cor}$	0.06	0.65
$M_{\rm BH}$	$f_{\rm pl}$	0.11	0.46
$M_{\rm BH}$	Γ	−0.383	0.005
$M_{\rm BH}$	$f_{\rm c}$	0.076	0.596
$L_{\rm X-ray}$	$L_{\rm torus}$	0.79	8.66×10^{-12}
$L_{\rm X-ray}$	κ_{2-10}	−0.29	0.04
$L_{\rm X-ray}$	$R_{\rm cor}$	0.05	0.71
$L_{\rm X-ray}$	$f_{\rm pl}$	0.27	0.06
$L_{\rm X-ray}$	Γ	−0.34	0.01
$L_{\rm X-ray}$	$f_{\rm c}$	0.007	0.96
$L_{\rm torus}$	κ_{2-10}	0.16	0.26
$L_{\rm torus}$	$R_{\rm cor}$	−0.234	0.098
$L_{\rm torus}$	$f_{\rm pl}$	0.09	0.55
$L_{\rm torus}$	Γ	−0.14	0.33
$L_{\rm torus}$	$f_{\rm c}$	0.17	0.22
κ_{2-10}	$R_{\rm cor}$	−0.65	2.31×10^{-07}
κ_{2-10}	$f_{\rm pl}$	−0.52	7.89×10^{-05}
κ_{2-10}	Γ	0.434	0.001
κ_{2-10}	$f_{\rm c}$	−0.378	0.007
$R_{\rm cor}$	$f_{\rm pl}$	−0.07	0.61
$R_{\rm cor}$	Γ	−0.31	0.03
$R_{\rm cor}$	$f_{\rm c}$	0.32	0.02
$f_{\rm pl}$	Γ	−0.29	0.04
$f_{\rm pl}$	$f_{\rm c}$	0.3	0.03
Γ	$f_{\rm c}$	−0.18	0.21

also their $f_{\rm c}$ values. When excluding the 13 sources for which $L_{\rm host}$ are not constrained, neither the scatter (∼0.17) nor the mean value (∼0.33) for the remaining 38 sources are changed significantly from the covering factors of the overall sample. This indicates that the uncertainties in $L_{\rm host}$ do not strongly bias our overall results.

5 DISCUSSION

The effect of the well-known *receding torus model* (Lawrence 1991) predicts that $f_{\rm c}$ decreases with increasing $L_{\rm Bol}$. Whilst our data marginally supports this prediction we find a stronger anticorrelation between $f_{\rm c}$ and $\lambda_{\rm Edd}$. So it is not clear which parameter (or both) is the fundamental driver of the trends seen. This is made more complex as $f_{\rm c} = L_{\rm torus}/L_{\rm Bol}$, so there is an implicit bias where $f_{\rm c}$ will anticorrelate with $L_{\rm Bol}$.

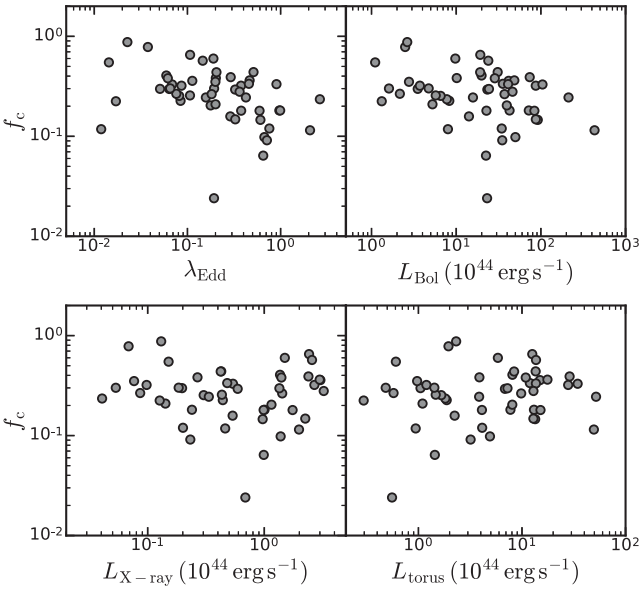

Figure 4. The variation of $f_{\rm c}$ with $\lambda_{\rm Edd}$ (upper left), $L_{\rm Bol}$ (upper right), $L_{\rm X-ray}$ (lower left) and $L_{\rm torus}$ (lower right).

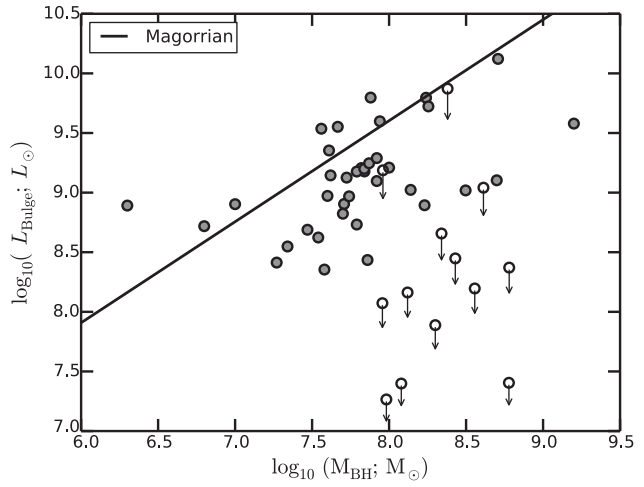

Figure 5. Plot showing the relationship between the bulge luminosity and the black hole mass. The circles are the data points and the solid black line describes the Margorrian relationship (Magorrian et al. 1998) for our data. The open circles with lower arrow denote the sources for which we have considered the upper limits of $L_{\rm host}$.

In order to investigate this, we carried out a simulation to predict the correlation between these parameters given in our sample. We generated 10 000 realizations of random data where pairs of $L_{\rm Bol}$ and $\lambda_{\rm Edd}$ are drawn from the data using bootstrap sampling with replacement and then assigned a redshift from the sample, z, again with replacement. A sample of 51 $f_{\rm c}$ values is produced from a uniform distribution within the range of 0.0–0.9, roughly corresponding to the observational range. This allows us to calculate the IR flux which would result from assuming a random distribution of covering fraction. We applied an effective IR detection threshold to the simulations, similar to what is expected for the data. We use the standard 12 μm limiting flux of 1 mJy for the *WISE* all-sky survey as our threshold (Wright et al. 2010). If the simulated IR flux is more than 1 mJy and the corresponding IR luminosity is within the range of the original data, the source is retained; otherwise, it

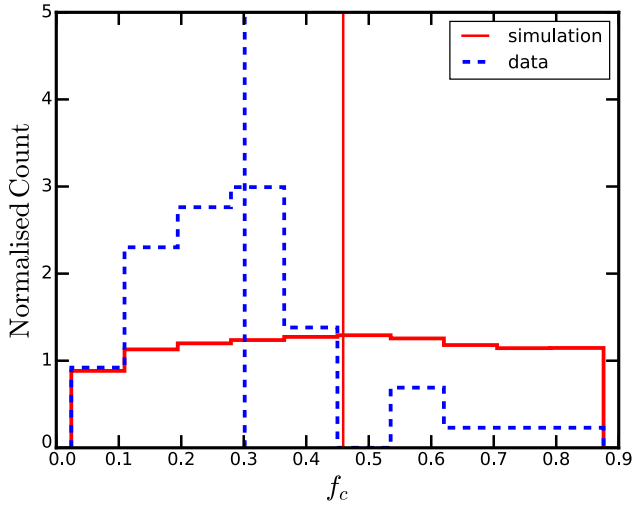

Figure 6. Histogram of f_c for the original sample (blue dashed line) and the simulation (red solid line). Blue (dashed) and red (solid) vertical lines show the mean values of the respective distributions of f_c.

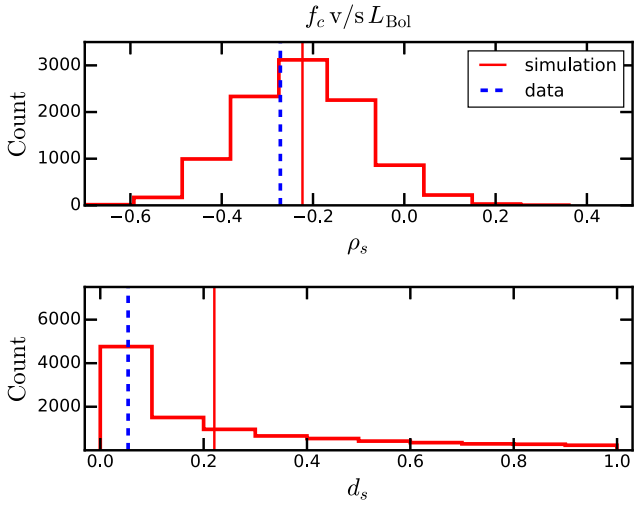

Figure 7. Histogram of ρ_s (upper panel) and d_s (lower panel) of Spearman's correlation between f_c and $L_{\rm Bol}$ for the simulation. The blue dashed line denotes ρ_s of the original data (upper panel), and ∼36 per cent of the realizations lie below this showing stronger anticorrelation than the original sample.

is discarded and new values of $L_{\rm Bol}$, $\lambda_{\rm Edd}$, z and f_c are drawn. We checked that this gives rise to realizations with the same distribution of $L_{\rm torus}$ as found in the actual data. There is a difference at the level of 0.02 according to the K–S test, which is only marginally significant. Further tests carried out with randomized log(f_c), make the difference even less significant. However, Fig. 6 shows that the distribution of f_c in the data is very different from the simulation, where an assumed initial random distribution is modified by the IR selection.

In each realization, we calculate the Spearman's correlation between $L_{\rm Bol}$ and f_c. The rank coefficient of the original data was −0.27, very similar to the value of $\rho_s \sim -0.29$ seen in the simulation, and ∼36 per cent of the realizations show an anticorrelation stronger than that found in the actual data (see Fig. 7). So, in our sample, there is no significant anticorrelation between $L_{\rm Bol}$ and f_c.

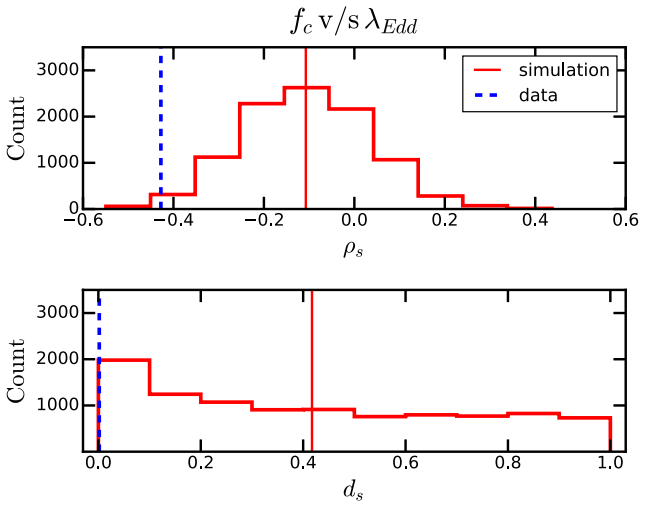

Figure 8. Histogram of ρ_s (upper panel) and d_s (lower panel) of Spearman's correlation between f_c and $\lambda_{\rm Edd}$ for 10 000 realizations. Here, only ∼1 per cent of the realizations show stronger anticorrelation than the original data.

We repeat this procedure for $\lambda_{\rm Edd}$ and f_c, but here the results are very different. The rank coefficient of ∼−0.43 seen in the data is very different to the rank coefficient of the simulation, with only ∼1 per cent of the realizations showing an anticorrelation stronger than that based on the original data (see Fig. 8), so this is significant at close to 3σ.

Thus f_c in our sample is not significantly correlated with $L_{\rm Bol}$, but it is with $\lambda_{\rm Edd}$ at ∼99 per cent significance. This indicates that changes in the covering factor are driven more by changes in the Eddington ratio, rather than by changes in the bolometric luminosity. This adds to a growing body of evidence that there are large-scale changes in the SED with $\lambda_{\rm Edd}$ (Vasudevan & Fabian 2007; Vasudevan & Fabian 2009; Lusso et al. 2013, J12a,b). Therefore, we find that the most basic of the unification models in which it is proposed that the observed AGN properties only depend on inclination are too simple, and there are changes in the shape of the SED which depend on $\lambda_{\rm Edd}$, as well as $M_{\rm BH}$ which sets the overall luminosity scale. However, the anticorrelation of the dust covering fraction with $\lambda_{\rm Edd}$ rather than $L_{\rm Bol}$ indicates a change in the larger scale geometry of the AGN rather than just the expected response of the dust to increasing illumination. Such a large-scale change may also be required to produce the observed anticorrelation of the forbidden series of the narrow emission lines with $\lambda_{\rm Edd}$, as NLS1s and other high $\lambda_{\rm Edd}$ AGN are known to have weak [O III] (e.g. Boroson & Meyers 1992; Done & Jin 2016). Furthermore, Leighly (2004) speculate that this is due to the very inner regions of the accretion flow being progressively shielded by a wind, with increasing $\lambda_{\rm Edd}$. Thereby even if there is copious dust present, the irradiated fraction decreases as the ionizing radiation becomes more collimated, and hence the reprocessed fraction drops. Fabian, Vasudevan & Gandhi (2008) have discussed the fact that efficient coupling of dust to gas boosts the effect of radiation pressure feedback. The result is that absorbed AGN are mostly found at low Eddington ratios. Here, we are seeing a decrease of the (illuminated) dust fraction in type 1 AGN. The effect could be related to that noted by Fabian et al. (2008) in absorbed AGN, with the feedback in our sample occurring out of our direct line of sight. Conversely, if the bulk of the MIR is emitted by dust located in the polar directions, then this

result relates to the relative efficiency of illuminated dust emission in the line of sight.

6 CONCLUSIONS

We present a detailed study of the dust covering factors for an X-ray/optically selected sample of unobscured type 1 AGN in the local Universe using the data available from *XMM–Newton*, SDSS, *WISE*, 2MASS and UKIDSS. We used the method of SED modelling analysis to determine the covering factor of each source. Two important aspects of this work are that we have broad-band spectra to determine $L_{\rm Bol}$, and a self-consistent model to estimate the contribution of the unobservable FUV region. We find a mean covering factor of $f_{\rm c} = 0.30$, with $0.02 < f_{\rm c} < 0.88$ and a dispersion of the individual values of $\sigma_f = 0.17$. The distribution shows a trend of anticorrelation with $\lambda_{\rm Edd}$ and $L_{\rm Bol}$, but further analysis based on simulations shows that only the trend with $\lambda_{\rm Edd}$ is significant at ∼99 per cent. This implies a large-scale change in the geometry of the illuminated dust, rather than simply to a response from increasing $L_{\rm Bol}$. Division into sub-samples of radio-loud AGN and NLS1, do not reveal any significant differences in the distribution of covering factors from the whole sample. This argues against the presence of a strong additional driving parameter for $f_{\rm c}$ in these sub-samples. However, the number of objects is small, and further studies are needed.

Our study is based on 51 sources, for which we have comprehensive multiwavelength coverage. It would be valuable to extend this type of study to a larger sample of AGN, with a wider range of redshifts to test the correlations we find and the conclusions that we have drawn. It is relevant to select sources with different combinations of black hole mass and accretion rate since the behaviour of the accretion disc spectrum depends on these parameters. Further extension of this study can be expected from *AstroSat* (Singh et al. 2014) which can obtain simultaneous observations in X-ray and UV bands.

ACKNOWLEDGEMENTS

We thank the referee Konrad Tristram for his thorough review and useful comments. We acknowledge the UGC-UKIERI Thematic Partnership 2015 (UGC 2014-15/02) for the support of the grant for this work. The first author is grateful to the Department of Science and Technology (No. SR/S2/HEP-07/2012) for the financial support. PG acknowledges the support of STFC (No. ST/J003697/2). CD acknowledges support under STFC grant ST/L00075X/1.

This work is based on observations obtained with *XMM–Newton*, an ESA science mission with instruments and contributions directly funded by ESA Member States and NASA. This research has made use of the NASA/IPAC Infrared Science Archive, which is operated by the Jet Propulsion Laboratory, California Institute of Technology, under contract with the National Aeronautics and Space Administration. This publication makes use of data products from the *Wide-field Infrared Survey Explorer*, which is a joint project of the University of California, Los Angeles, and the Jet Propulsion Laboratory/California Institute of Technology, funded by the National Aeronautics and Space Administration. We have used the UKIDSS data from Data Release 10. The UKIDSS project is defined in (Lawrence et al. 2007). UKIDSS uses the UKIRT Wide Field Camera (WFCAM; Casali et al. 2007). The photometric system is described in Hewett et al. (2006), and the calibration is described in Hodgkin et al. (2009). The pipeline processing and science archive are described in Hambly et al. (2008). This publication makes use of data products from the Two Micron All Sky Survey, which is a joint project of the University of Massachusetts and the Infrared Processing and Analysis Center/California Institute of Technology, funded by the National Aeronautics and Space Administration and the National Science Foundation.

Funding for the SDSS and SDSS-II has been provided by the Alfred P. Sloan Foundation, the Participating Institutions, the National Science Foundation, the U.S. Department of Energy, the National Aeronautics and Space Administration, the Japanese Monbukagakusho, the Max Planck Society, and the Higher Education Funding Council for England. The SDSS Web Site is http://www.sdss.org/.

The SDSS is managed by the Astrophysical Research Consortium for the Participating Institutions. The Participating Institutions are the American Museum of Natural History, Astrophysical Institute Potsdam, University of Basel, University of Cambridge, Case Western Reserve University, University of Chicago, Drexel University, Fermilab, the Institute for Advanced Study, the Japan Participation Group, Johns Hopkins University, the Joint Institute for Nuclear Astrophysics, the Kavli Institute for Particle Astrophysics and Cosmology, the Korean Scientist Group, the Chinese Academy of Sciences (LAMOST), Los Alamos National Laboratory, the Max-Planck-Institute for Astronomy (MPIA), the Max-Planck-Institute for Astrophysics (MPA), New Mexico State University, Ohio State University, University of Pittsburgh, University of Portsmouth, Princeton University, the United States Naval Observatory and the University of Washington.

This research has made use of the NASA/IPAC Extragalactic Database (NED) which is operated by the Jet Propulsion Laboratory, California Institute of Technology, under contract with the National Aeronautics and Space Administration.

REFERENCES

Antonucci R., 1993, ARA&A, 31, 473
Appenzeller I. et al., 1998, ApJS, 117, 319
Asmus D., Hönig S. F., Gandhi P., 2016, ApJ, 822, 109
Barvainis R., 1987, ApJ, 320, 537
Boroson T. A., Meyers K. A., 1992, ApJ, 397, 442
Burtscher L. et al., 2013, A&A, 558, A149
Cardelli J. A., Clayton G. C., Mathis J. S., 1989, ApJ, 345, 245
Casali M. et al., 2007, A&A, 467, 777
Collinson J. S., Ward M. J., Landt H., Done C., Elvis M., McDowell J. C., 2016, MNRAS, 465, 358
Done C., Jin C., 2016, MNRAS, 460, 1716
Done C., Davis S. W., Jin C., Blaes O., Ward M., 2012, MNRAS, 420, 1848
Dwelly T., Page M. J., 2006, MNRAS, 372, 1755
Eckart M. E., Stern D., Helfand D. J., Harrison F. A., Mao P. H., Yost S. A., 2006, ApJS, 165, 19
Elvis M. et al., 1994, ApJS, 95, 1
Fabian A. C., Vasudevan R. V., Gandhi P., 2008, MNRAS, 385, L43
Gallagher S. C., Richards G. T., Lacy M., Hines D. C., Elitzur M., Storrie-Lombardi L. J., 2007, ApJ, 661, 30
Gandhi P., Horst H., Smette A., Hönig S., Comastri A., Gilli R., Vignali C., Duschl W., 2009, A&A, 502, 457
Gandhi P. et al., 2011, ApJ, 740, L13
Haardt F., Maraschi L., 1993, ApJ, 413, 507
Hambly N. C. et al., 2008, MNRAS, 384, 637
Hao L. et al., 2005, AJ, 129, 1795
Hao H. et al., 2010, ApJ, 724, L59
Hasinger G., 2008, A&A, 490, 905
Hatziminaoglou E. et al., 2008, MNRAS, 386, 1252
Hatziminaoglou E., Fritz J., Jarrett T. H., 2009, MNRAS, 399, 1206

Hewett P. C., Warren S. J., Leggett S. K., Hodgkin S. T., 2006, MNRAS, 367, 454
Hodgkin S. T., Irwin M. J., Hewett P. C., Warren S. J., 2009, MNRAS, 394, 675
Hönig S. F., Kishimoto M., 2010, A&A, 523, A27
Hönig S. F. et al., 2013, ApJ, 771, 87
Jin C., Ward M., Done C., Gelbord J., 2012a, MNRAS, 420, 1825 (J12a)
Jin C., Ward M., Done C., 2012b, MNRAS, 425, 907 (J12b)
Jin C., Done C., Ward M., 2016, MNRAS, 455, 691
Kalberla P. M. W., Burton W. B., Hartmann D., Arnal E. M., Bajaja E., Morras R., Pöppel W. G. L., 2005, A&A, 440, 775
Khorunzhev G. A., Sazonov S. Y., Burenin R. A., Tkachenko A. Y., 2012, Astron. Lett., 38, 475
Kishimoto M., Hönig S. F., Beckert T., Weigelt G., 2007, A&A, 476, 713
La Franca F. et al., 2005, ApJ, 635, 864
Landt H., Elvis M., Ward M. J. Bentz M. C., Korista K. T., Karovska M., 2011, MNRAS, 414, 218
Lawrence A., 1991, MNRAS, 252, 586
Lawrence A., Elvis M., 2010, ApJ, 714, 561
Lawrence A. et al., 2007, MNRAS, 379, 1599
Leighly K. M., 2004, ApJ, 611, 125
López-Gonzaga N., Burtscher L., Tristram K. R. W., Meisenheimer K., Schartmann M., 2016, A&A, 591, A47
Lusso E. et al., 2013, ApJ, 777, 86
Magorrian J. et al., 1998, AJ, 115, 2285
Maiolino R., Shemmer O., Imanishi M., Netzer H., Oliva E., Lutz D., Sturm E., 2007, A&A, 468, 979
Mateos S. et al., 2012, MNRAS, 426, 3271
Mateos S. A. et al., 2016, ApJ, 819, 166
Mor R., Trakhtenbrot B., 2011, ApJ, 737, L36
Mor R., Netzer H., Elitzur M., 2009, ApJ, 705, 298
Mullaney J. R., Alexander D. M., Goulding A. D., Hickox R. C., 2011, MNRAS, 414, 1082 (M11)
Nenkova M., Sirocky M. M., Nikutta R., Ivezić Ž., Elitzur M., 2008, ApJ, 685, 160
Netzer H., 2013, The Physics and Evolution of Active Galactic Nuclei. Cambridge Univ. Press, Cambridge
Netzer H., 2015, ARA&A, 53, 365
Pier E. A., Krolik J. H., 1992, ApJ, 401, 99
Polletta M. et al., 2007, ApJ, 663, 81
Press W. H., Teukolsky S. A., Vetterling W. T., Flannery B. P., 1992, Numerical recipes in fortran. The art of scientific computing. Cambridge Univ. Press, Cambridge
Richstone D. O., Schmidt M., 1980, ApJ, 235, 361
Risaliti G., Maiolino R., Salvati M., 1999, ApJ, 522, 157
Roseboom I. G., Lawrence A., Elvis M., Petty S., Shen Y., Hao H., 2013, MNRAS, 429, 1494
Sanders D. B., Phinney E. S., Neugebauer G., Soifer B. T., Matthews K., 1989, ApJ, 347, 29
Silva L., Maiolino R., Granato G. L., 2004, MNRAS, 355, 973
Simpson C., 2005, MNRAS, 360, 565
Singh K. P. et al., 2014, in Takahashi T., den Herder J.-W. A., Bautz M., eds, Proc. SPIE Conf. Ser. Vol. 9144, Space Telescopes and Instrumentation 2014: Ultraviolet to Gamma Ray. SPIE, Bellingham, p. 91441S
Skrutskie M. F. et al., 2006, AJ, 131, 1163
Stalevski M., Ricci C., Ueda Y., Lira P., Fritz J., Baes M., 2016, MNRAS, 458, 2288
Steffen A. T., Barger A. J., Cowie L. L., Mushotzky R. F., Yang Y., 2003, ApJ, 596, L23
Stern D. et al., 2012, ApJ, 753, 30
Suganuma M. et al., 2006, ApJ, 639, 46
Toba Y. et al., 2013, PASJ, 65, 113
Treister E., Urry C. M., 2006, ApJ, 652, L79
Treister E., Krolik J. H., Dullemond C., 2008, ApJ, 679, 140
Tueller J. et al., 2010, ApJS, 186, 378
Ueda Y., Akiyama M., Ohta K., Miyaji T., 2003, ApJ, 598, 886
Urry C. M., Padovani P., 1995, PASP, 107, 803
Vasudevan R. V., Fabian A. C., 2007, MNRAS, 381, 1235
Vasudevan R. V., Fabian A. C., 2009, MNRAS, 392, 1124
Wright E. L. et al., 2010, AJ, 140, 1868

APPENDIX A: IR SED TEMPLATES

A1 *agndust* templates

The model *agndust* makes use of the templates from Silva et al. (2004) who derived the nuclear infrared spectral energy distributions for a sample of obscured and unobscured Seyfert galaxies. They divided the observed IR SEDs into intervals of intrinsic absorbing column density $N_{\rm H}$. In order to exclude the objects with $N_{\rm H} > 10^{25}$ cm^{-2} these SEDs were already normalized by the unabsorbed hard X-ray (2–10 keV band) flux. They obtained four different SEDs averaged within bins of absorbing $N_{\rm H}$. One among these nuclear IR SEDs corresponds to Seyfert 1 objects with $N_{\rm H} < 10^{22}$ cm^{-2} and the other three SEDs are for Seyfert 2 galaxies with $10^{22} < N_{\rm H} < 10^{23}$ cm^{-2}, $10^{23} < N_{\rm H} < 10^{24}$ cm^{-2} and $10^{24} < N_{\rm H} < 10^{25}$ cm^{-2}. The *agndust* model can make use of the four SEDs for modelling the IR data. In view of our sample selection, we make use of only the Seyfert 1 template by excluding the part of the SED at shorter wavelengths, plotted in blue in Fig. A1.

A2 *hostpol* templates

The *hostpol* component uses the IR SED templates from the SWIRE template library (Polletta et al. 2007). The SWIRE template library has 25 IR SED templates which cover the wavelength range between 1000 Å and 1000 μm. The library consists of six ellipticals, seven spirals, six starbursts, seven AGN and two composite (starburst+AGN) templates. The AGN templates comprise three type 1 and four type 2 AGN SEDs. The 13 SWIRE templates we used for modelling the host galaxy IR emission using *hostpol* model (See Table A1) are plotted in Fig. A2.

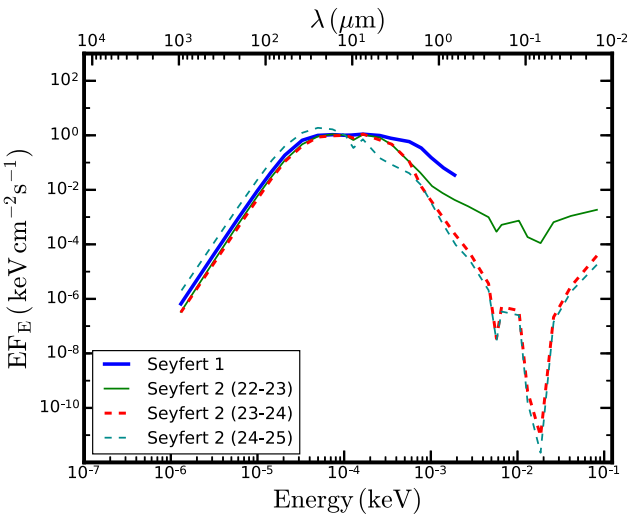

Figure A1. The rest-frame Silva SED templates (Silva et al. 2004) for Seyfert 1 and Seyfert 2 galaxies, normalized at 12 μm. Seyfert 2 (22–23), Seyfert 2 (23–24) and Seyfert 2 (24–25) denote SEDs with $10^{22} < N_H < 10^{23}$ cm^{-2}, $10^{23} < N_H < 10^{24}$ cm^{-2} and $10^{24} < N_H < 10^{25}$ cm^{-2}, respectively. We isolate the infrared hump of the Seyfert 1 SED to concentrate on the dust reprocessing component of the torus.

Table A1. *hostpol* model components and corresponding SED templates of host galaxies used in our analysis (*starburst galaxies).

hostpol component	SED template
*host*01	S0
*host*02	Sa
*host*03	Sb
*host*04	Sc
*host*05	Sd
*host*06	E2
*host*07	E5
*host*08	NGC 6090*
*host*09	NGC 6240*
*host*10	M 82*
*host*11	Arp 220*
*host*12	IRAS 22491−1808*
*host*13	IRAS 20551−4250*

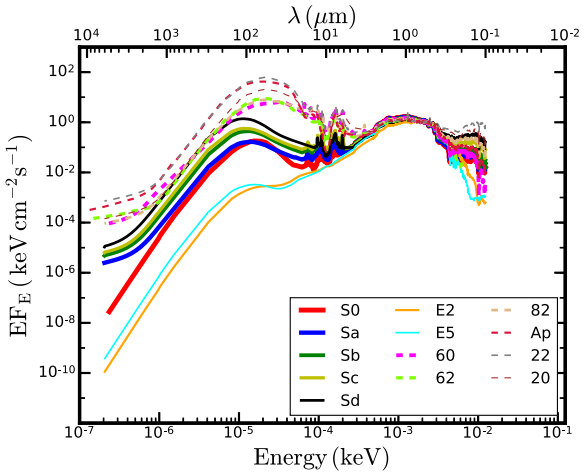

Figure A2. The host galaxy SEDs from Polletta et al. 2007 (flux density normalised at 5500 Å) for spirals (S0–Sd), ellipticals (E2 & E5) and starburst galaxies. The starburst templates correspond to the SEDs of NGC 6090 (60), NGC 6240 (62), M 82 (82), Arp 220 (Ap), IRAS 22491−1808 (22), and IRAS 20551−4250 (20).

APPENDIX B: BROAD-BAND SED FITS

The broad-band SED fits for the complete sample are shown in Fig. B1.

APPENDIX C: NOTES ON INDIVIDUAL SOURCES

C1 Discrepancies in SDSS data

The SDSS data points in the SEDs of the objects Mrk 0110 (No. 9), PG 0947+396 (No. 10), PG 1202+281 (No. 21), LBQS 1228+1116 (No. 25), PG 1244+026 (No. 30), RBS 1201 (No. 32), PG 1415+451 (No. 40), NGC 5683 (No. 42), PG 1512+370 (No. 45) and PG 2233+134 (No. 50) show some clear deviations from the broad-band continuum model. This may be attributed to the intrinsic variability of the sources. Since the observations of SDSS and OM are not simultaneous, there may be some discrepancy between the two data sets. The SED of Mrk 0110 shows large offset in the SDSS data points. J12a discussed this source and mentioned that it is an extreme example of this behaviour. In order to check the influence of the discrepancy, we fit these sources with the same model without using the SDSS data. We observed that f_c remain unchanged in eight sources, and in only two cases [PG 0947+396 (No. 10) & PG 1202+281 (No. 21)], there is a drop by a factor of ∼2.

C2 Sources with multiple *hostpol* templates

In the case of Mrk 0110 (No. 9) and PG 1115+407 (No. 18), the normalizations of all *hostpol* templates are nearly zero and are equally fitted by multiple host galaxy templates. For Mrk 0110, all the *hostpol* templates provide the same fit-statistic and even the same spectral parameters. However, Mrk 0110 is identified as an Sa galaxy (Khorunzhev et al. 2012). Hence, in the main text, we mentioned the SED of spiral galaxy type-a (*host*02) as the best-fitting *hostpol* model for this object. In the case of PG 1115+407, more than one *hostpol* template gave the same χ^2 and slightly different parameter values. However, the morphological type of the source is unknown. In this case, we have adopted S0 template as the best-fitting component.

C3 Super-Eddington sources

There are two sources in our sample, KUG 1031+398 (No. 15) and PG 2233+134 (No. 50), which have super-Eddington accretion rates. Among these KUG 1031+398 has the highest value of $\lambda_{\rm Edd}$ (∼2.64) and lowest black hole mass, whereas PG 2233+134 has the highest value of bolometric luminosity. In these sources, we attempt to fit the data by fixing $\lambda_{\rm Edd}$ to 1 and letting $M_{\rm BH}$ be a free parameter. For KUG 1031+398 this resulted in an improvement in the fit ($\Delta\chi^2 = -58.5$) for a change in $M_{\rm BH}$ from $1.7 \times 10^6\ M_\odot$ to $3.8 \times 10^6\ M_\odot$. Here, the covering factor increased from 0.23 to 0.34. As discussed by Jin, Done & Ward (2016) this may be a super-Eddington source and the black hole mass obtained from the SED fitting may not be correct. In such sources, the super-Eddington flow may not be well fitted by a model that conserves energy. In the case of PG 2233+134, $M_{\rm BH}$ remained unchanged while χ^2(/dof) increased from 893.6(/173) to 2641.2(/173). In this case also, f_c shows an increase from 0.11 to 0.22. Although the inclination effects are not taken into account, it seems likely that this AGN is indeed a super-Eddington source. It is perhaps surprising that we are able to fit it as a super-Eddington source since such high Eddington sources probably power strong winds. So energy conservation is not appropriate due to loss of radiative power to the wind.

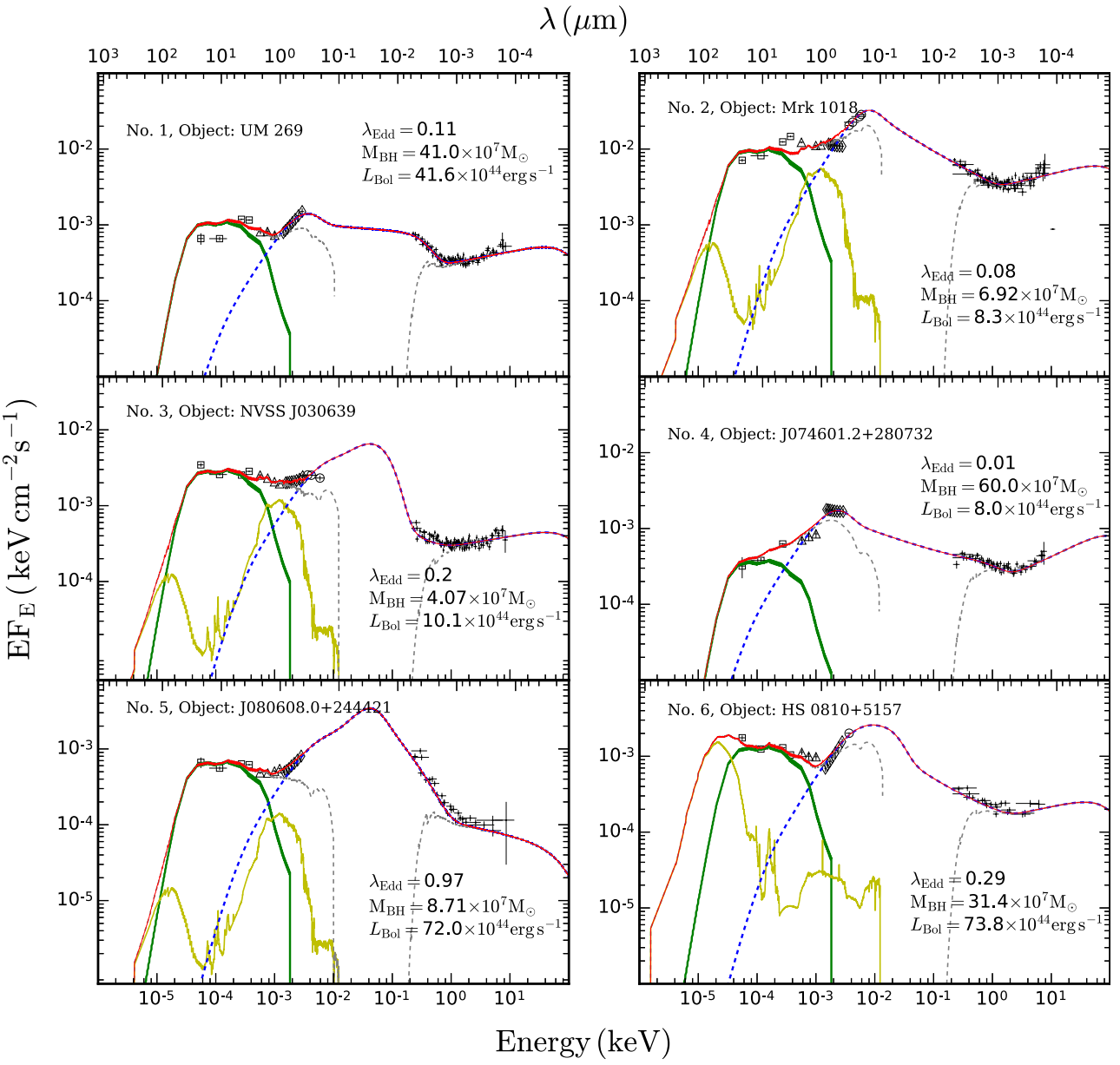

Figure B1. The broad-band SED fitting plots for the 51 sources. We fit the absorbed SEDs to the observed data and the resultant best-fitting models are shown in dashed grey line. However, we are mainly concerned with the measurements of $L_{\rm Bol}$, for which we illustrate the intrinsic model (solid red) together with the de-absorption corrections applied to the data. The individual model components OPTXAGNF, *agndust* and *hostpol* are plotted in dashed blue, solid green and solid yellow, respectively. Data from *XMM–Newton* EPIC, Optical Monitor, SDSS, UKIDSS/2MASS, and *WISE* are respectively represented by black dots, circles, diamonds, triangles and squares. X-ray data have been rebinned for plotting purpose.

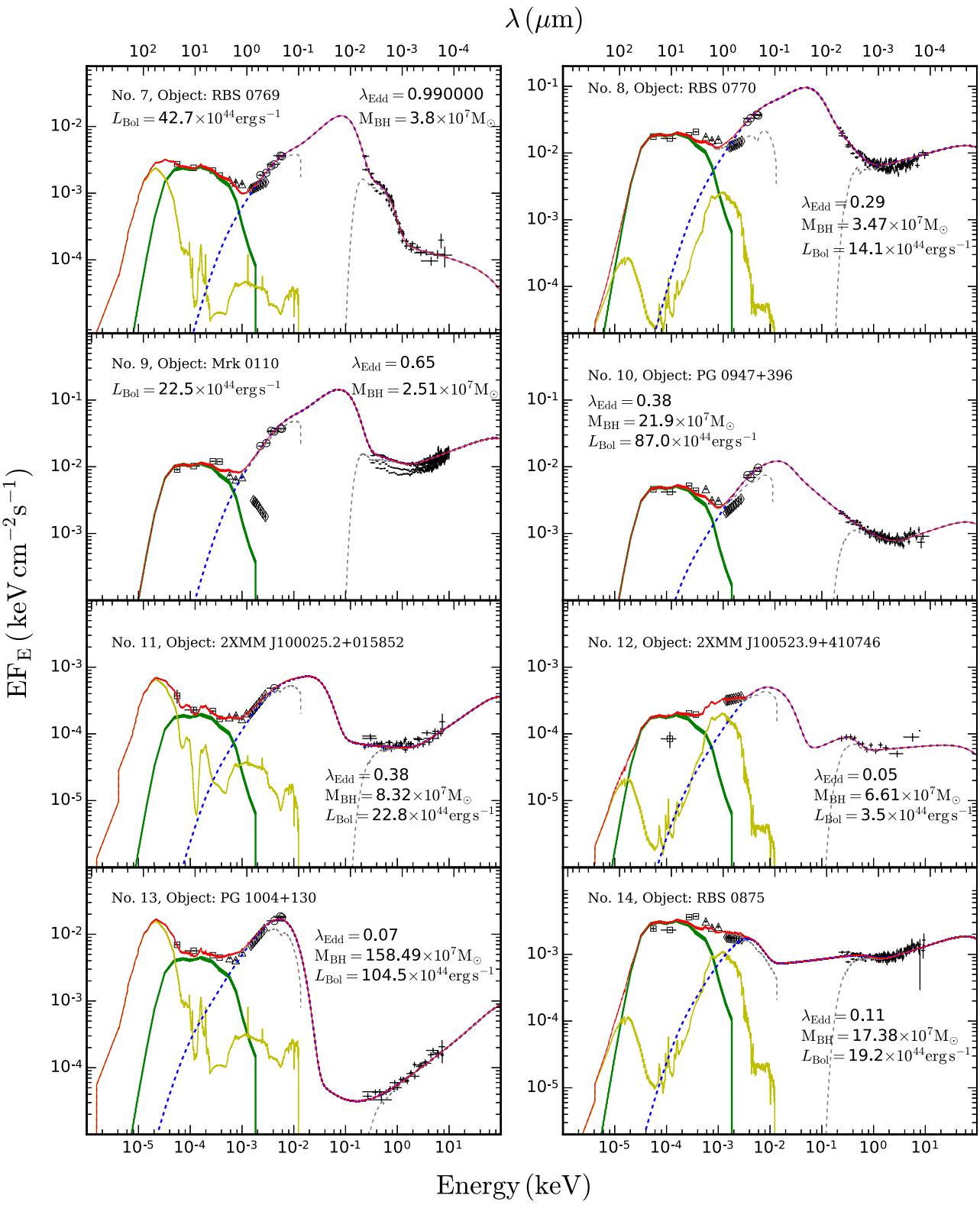

Figure B1 – *continued*

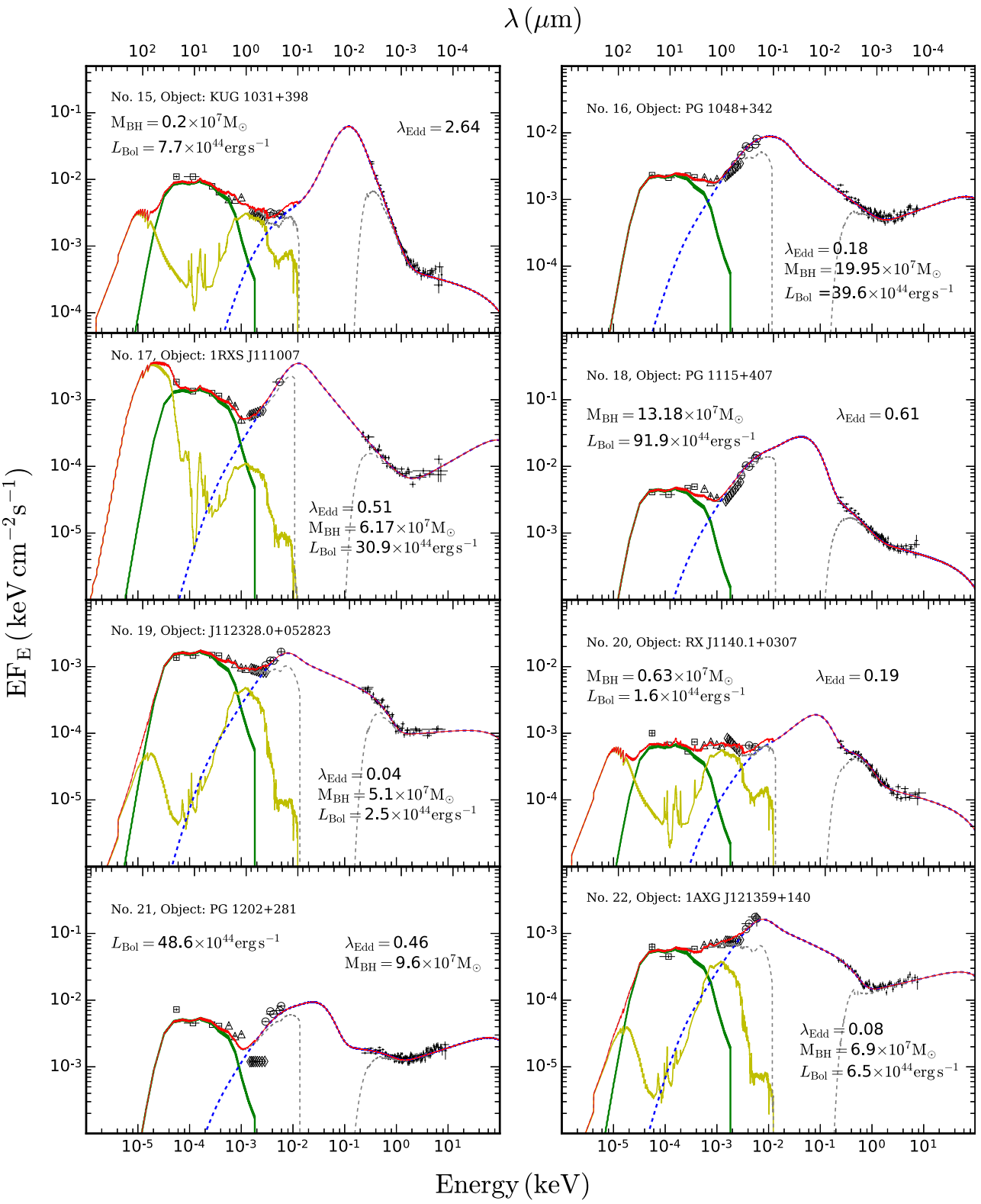

Figure B1 – *continued*

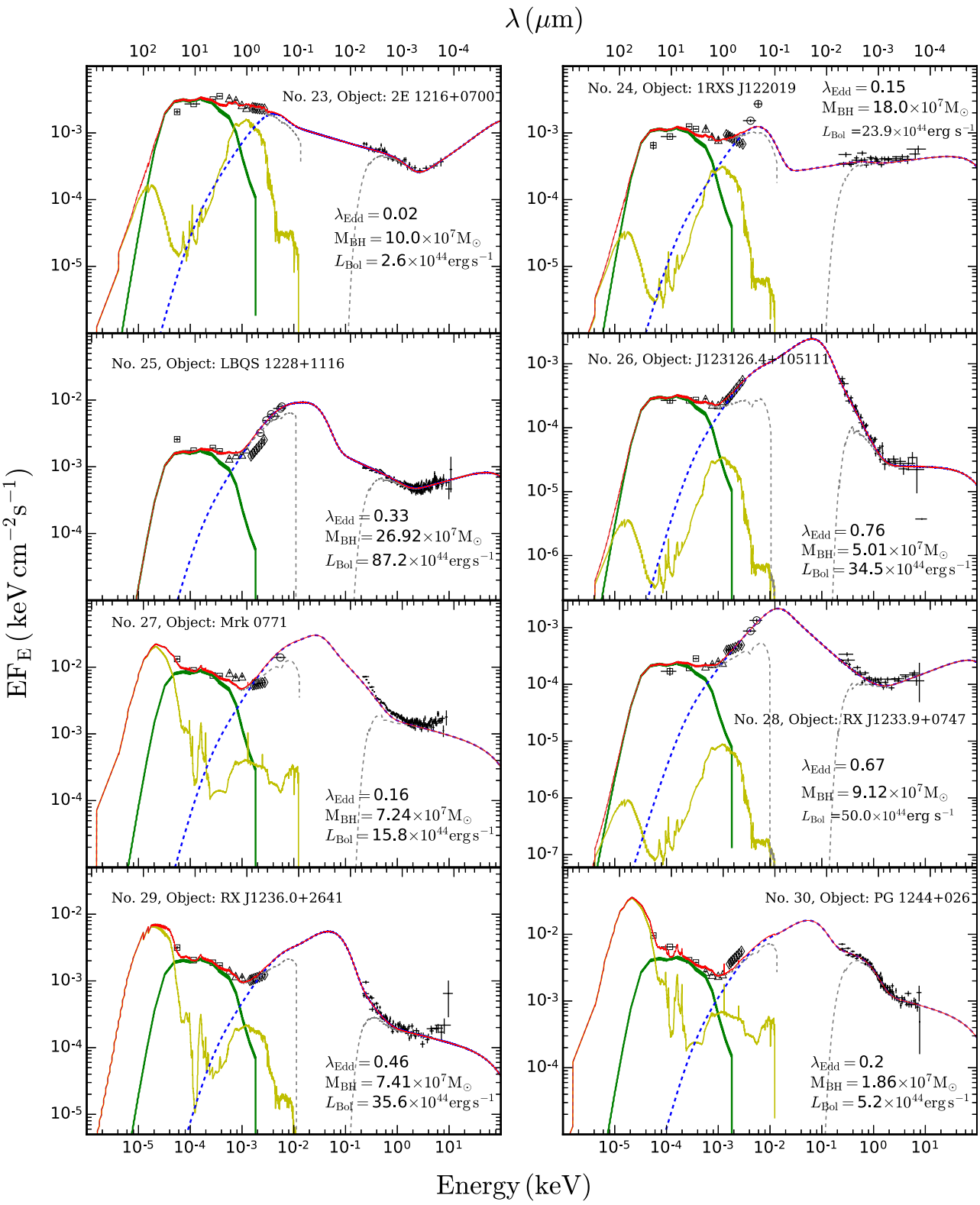

Figure B1 – *continued*

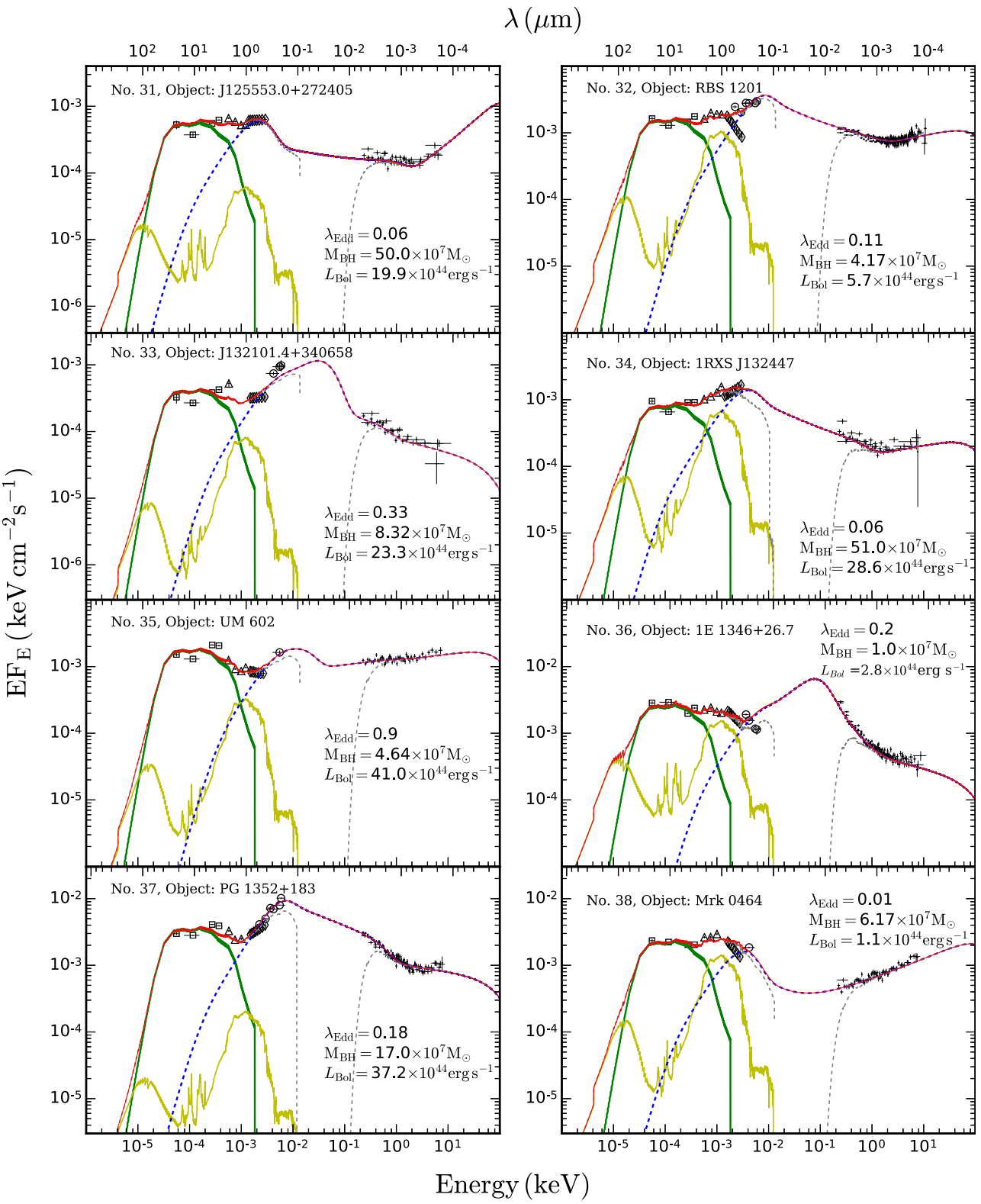

Figure B1 – *continued*

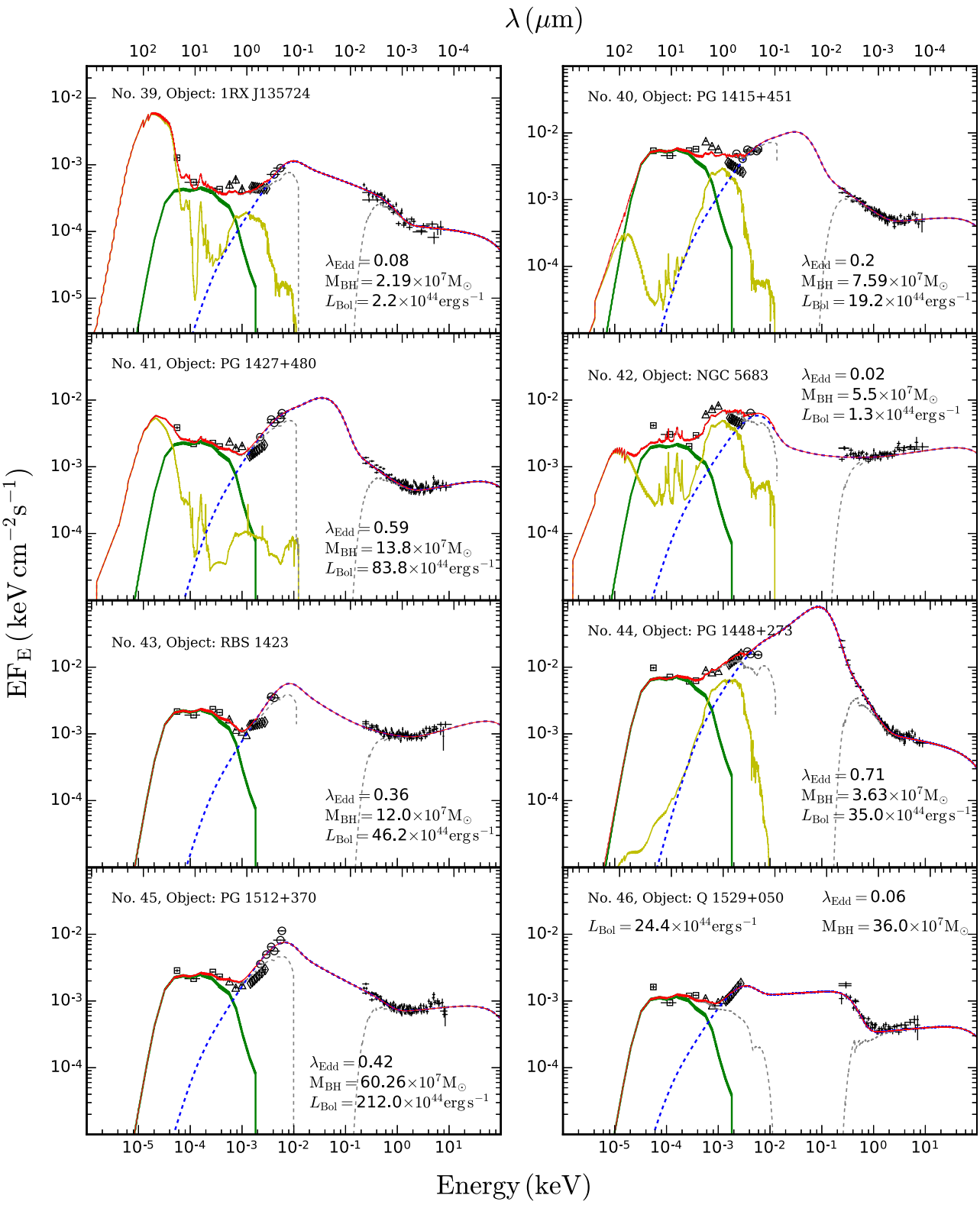

Figure B1 – *continued*

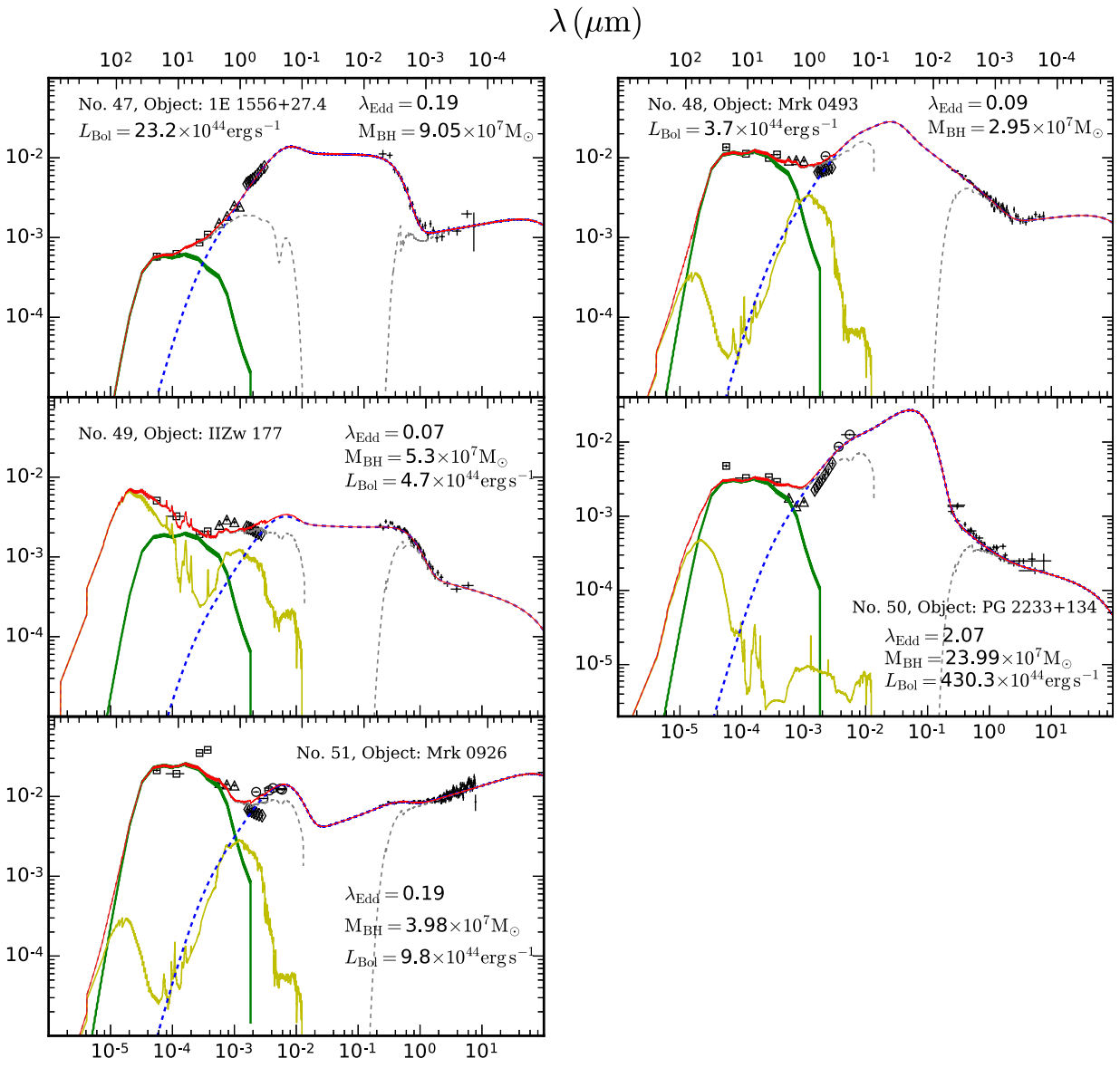

Figure B1 – *continued*

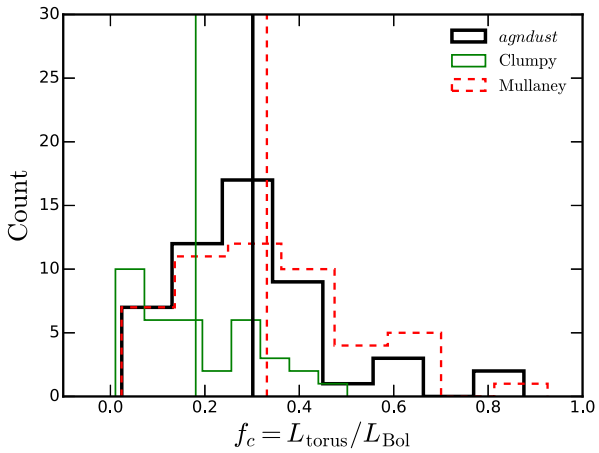

Figure D1. Histograms of covering factors for *agndust* SED (thick black line), extended M11 SED (dashed red line) and Clumpy SED for type 1 AGN (thin green line). The vertical lines represent the mean values of f_c for different distributions.

APPENDIX D: OTHER TORUS TEMPLATES

Mullaney et al. (2011) (hereafter M11) have constructed a range of intrinsic MIR to FIR (6–100 μm) SEDs of a sample of X-ray selected local AGN with moderate luminosities. We have fitted our sample with M11 SED by extending it down to about 0.6 μm to match the range of our *agndust* (Silva et al. 2004) template for Seyfert 1. The covering factors obtained with this template have a very similar range, mean and scatter as that for *agndust*. Although the SED fits and spectral parameters are comparable to that of *agndust*, for most of the sources the fit resulted in comparatively poor χ^2. This is probably due to the fact that the extended M11 SED is narrow and so fails to cover the peak in emission around the NIR region.

We have also attempted fitting the data with Clumpy SED for type 1 AGN (Hönig & Kishimoto 2010) with inclination 30 degrees, by modifying the template to match the wavelength range of *agndust*. But again we note that the template is narrow compared to *agndust* SED, and peaks around 10 μm. Also, the torus luminosity for this component over 1–1000 μm is a factor of ∼1.3 lower than that for *agndust* SED. The fits provide poor statistic for ∼70 per cent of the sources in the sample and a lower range of covering factors ∼0.01–0.5 with a mean around 0.18.

The data appear to require an extra hot dust component in the NIR, not covered by the above templates. We tested this for UM 269 (No. 1) by adding a black body component (XSPEC model *bbody*) with temperature ∼1000–1500 K. For this source, a black body with ∼1000 K temperature in the NIR region, in addition to the Clumpy SED provided a better χ^2 and resulted in a similar covering factor (∼0.31) as we obtained when using *agndust*. Hence the overall results are consistent with those obtained before.

The histograms of covering factors obtained for *agndust*, extended M11 and Clumpy SEDs are shown in Fig. D1.

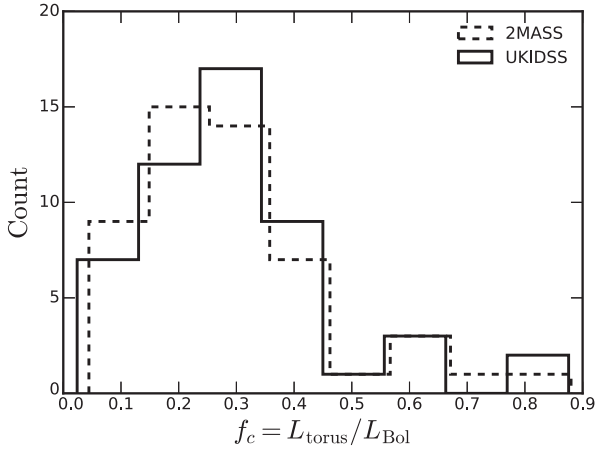

Figure E1. Distributions of covering factors obtained using 2MASS data (dashed line) and UKIDSS data (solid line) for the NIR band.

APPENDIX E: ANALYSIS WITH 2MASS DATA

As mentioned in Section 2.1, we opted to use NIR data from UKIDSS instead of 2MASS because of the smaller aperture size of the UKIDSS camera (2arcsec diameter for UKIDSS and 4arcsec radius for 2MASS), which therefore reduces the contribution from the host galaxy. Also, three sources in our sample lack 2MASS data and in those cases we require UKIDSS data. However, for comparison, we have analysed the entire sample by fitting the broad-band SED with 2MASS data (if available) for the NIR band. We find that the distribution of covering factors is similar to that obtained when using the UKIDSS data. Both distributions of f_c have the same mean and standard deviation. The histograms of f_c are shown in Fig. E1. We have also checked the correlation of f_c with $L_{\rm Bol}$ and $\lambda_{\rm Edd}$ obtained for 2MASS data. The trend of f_c between these parameters is essentially the same as we found when using the UKIDSS data.

This paper has been typeset from a TEX/LATEX file prepared by the author.